Journal of
Instrumentation

OPEN ACCESS

Test beam demonstration of silicon microstrip modules with transverse momentum discrimination for the future CMS tracking detector

To cite this article: W. Adam *et al* 2018 *JINST* **13** P03003

View the article online for updates and enhancements.

You may also like

- A measurement of material in the ATLAS tracker using secondary hadronic interactions in 7 TeV *pp* collisions
M. Aaboud, G. Aad, B. Abbott et al.
- Experimental study of different silicon sensor options for the upgrade of the CMS Outer Tracker
W. Adam, T. Bergauer, D. Blöch et al.
- Pileup mitigation at CMS in 13 TeV data
A.M. Sirunyan, A. Tumasyan, W. Adam et al.

This content was downloaded from IP address 192.167.204.253 on 16/09/2025 at 07:28

Published by IOP Publishing for Sissa Medialab

Received: *November 13, 2017*
Accepted: *February 9, 2018*
Published: *March 6, 2018*

Test beam demonstration of silicon microstrip modules with transverse momentum discrimination for the future CMS tracking detector

The CMS Tracker collaboration

E-mail: ali.harb@desy.de

Abstract: A new CMS Tracker is under development for operation at the High Luminosity LHC from 2026 onwards. It includes an outer tracker based on dedicated modules that will reconstruct short track segments, called stubs, using spatially coincident clusters in two closely spaced silicon sensor layers. These modules allow the rejection of low transverse momentum track hits and reduce the data volume before transmission to the first level trigger. The inclusion of tracking information in the trigger decision is essential to limit the first level trigger accept rate. A customized front-end readout chip, the CMS Binary Chip (CBC), containing stub finding logic has been designed for this purpose. A prototype module, equipped with the CBC chip, has been constructed and operated for the first time in a 4 GeV/*c* positron beam at DESY. The behaviour of the stub finding was studied for different angles of beam incidence on a module, which allows an estimate of the sensitivity to transverse momentum within the future CMS detector. A sharp transverse momentum threshold around 2 GeV/*c* was demonstrated, which meets the requirement to reject a large fraction of low momentum tracks present in the LHC environment on-detector. This is the first realistic demonstration of a silicon tracking module that is able to select data, based on the particle's transverse momentum, for use in a first level trigger at the LHC. The results from this test are described here.

Keywords: Front-end electronics for detector readout; Particle tracking detectors; Trigger concepts and systems (hardware and software); Trigger detectors

© 2018 CERN for the benefit of the CMS collaboration. Published by IOP Publishing Ltd on behalf of Sissa Medialab. Original content from this work may be used under the terms of the Creative Commons Attribution 3.0 licence. Any further distribution of this work must maintain attribution to the author(s) and the title of the work, journal citation and DOI.

https://doi.org/10.1088/1748-0221/13/03/P03003

2018 JINST 13 P03003

Contents

1 Introduction **1**

2 Module hardware **2**
- 2.1 2S-p_T module concept 2
- 2.2 The CBC2 chip 4
- 2.3 Prototype mini-modules 6
- 2.4 Beam test module construction 6

3 Experimental setup **7**
- 3.1 Data acquisition 7
- 3.2 Calibration tasks 9
- 3.3 Recorded data sets 10

4 Event reconstruction **10**
- 4.1 Noise suppression 11
- 4.2 Offline reconstruction 11
- 4.3 Latency adjustment 12
- 4.4 TDC phase 13
- 4.5 Threshold determination 14
- 4.6 Alignment of the DUT 16

5 Beam parameters **16**

6 Results **17**
- 6.1 Cluster width 18
- 6.2 Cluster efficiency 19
- 6.3 Stub efficiency 22

7 Summary **24**

The CMS collaboration **27**

2018 JINST 13 P03003

1 Introduction

The planned upgrade of the LHC to the High Luminosity LHC (HL-LHC) in the next decade foresees an increase of the instantaneous luminosity in proton-proton collisions by an order of magnitude. The luminosity will reach up to $7.5 \times 10^{34}\,\mathrm{cm^{-2}s^{-1}}$, yielding about 200 collisions per bunch crossing with 25 ns bunch spacing, and aiming at a total integrated luminosity of about $3000\mathrm{fb}^{-1}$ [1]. This will significantly increase the statistical power of the data and extend the physics reach, but also requires major improvements to the experiments to cope with increased rates and occupancies, as well as increased radiation induced damage in the detector material.

An important implication of the corresponding upgrade programme, the Phase-II upgrade [2], is the replacement of the entire Silicon Strip Tracker of the CMS [3] experiment. Besides demands on occupancy and radiation hardness, it is essential to provide tracking information to the first level trigger (L1) in order to limit the event selection rate to the proposed future L1 accept rate of 750 kHz.

The concept of the future CMS tracker [4] is based on modules consisting of two closely-spaced silicon sensors read out by common front-end ASICs, which allow on-detector transverse momentum (p_T) discrimination of tracks. The key L1 functionality of these so-called 'p_T modules' is based on data reduction by identification of high-p_T tracks by coincidence of signals on both sensors. At inner radii from 20 cm to 60 cm, the two layers of each module are composed of one macro-pixel and one strip sensor (PS-p_T module), while at outer radii they are equipped with two strip sensors of identical design (2S-p_T module). In addition to the bits transporting the coincidence information, which will be sent off-detector at 40 MHz to be used by L1, independent transmission of the full signal information from each module is foreseen for all events following a L1 accept. A summary of this concept can be found in ref. [5] and its references.

A similar concept has also been proposed by the ATLAS [6] experiment and demonstrated in an electron beam using the ABC130 ASIC, with the correlation logic implemented on an external FPGA [7]. However this approach does not currently form part of the baseline for the ATLAS Phase-II tracker upgrade.

The readout of the silicon modules uses a binary architecture. New chips are being specifically designed for the p_T-discrimination logic. For the 2S-p_T modules, the CMS Binary Chip (CBC) was the first prototype for the strip module readout [8]; it was wire-bonded to a single strip sensor and operated in a previous test beam [9].

A second version of the CBC chip, the CBC2, has been bump-bonded to a hybrid, which is wire-bonded to two closely-spaced sensors, forming the first prototype of a full 2S-p_T module. This paper describes details of this 2S-p_T module prototype, the setup, and the results of the first test beam measurement carried out in November 2013. These studies comprise the module calibration, the performance using the offline data, and the efficiency of the trigger logic.

2 Module hardware

In this section, the concept of p_T-discrimination with a 2S-p_T module and the module design foreseen for the future CMS tracker are introduced. Then the hardware used in the test beam is described, including the relevant features of the CBC2, the prototype module specifications and the test device construction.

2.1 2S-p_T module concept

In the 3.8 T magnetic field of CMS, charged particles follow a curved trajectory transverse to the beam axis with the bending radius depending on the p_T of the particle. The concept of p_T discrimination in a 2S-p_T module is illustrated in figure 1. The dependence of the curvature on the particle momentum allows the definition of a search window whose boundaries define a certain p_T. The window is seeded by a signal on the bottom sensor. If a signal is found on the top sensor within the window, this short track segment formed from the signals on both sensors passes the

2018 JINST 13 P03003

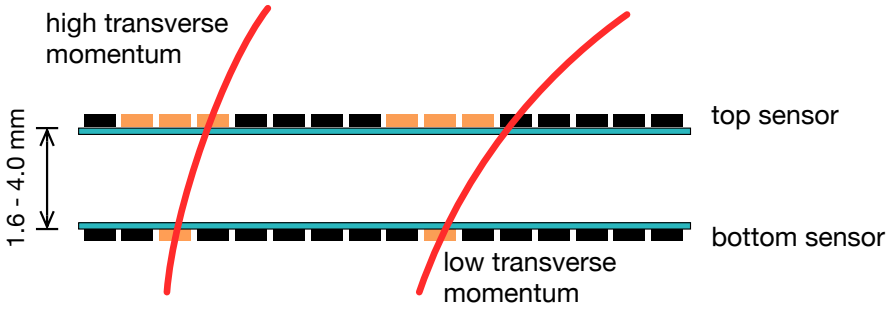

Figure 1. Concept of p_T-discrimination in a 2S-p_T module, using a search window size of ±1 strip on the top sensor, seeded by a signal on the bottom sensor. Shown are curved trajectories, one of high transverse momentum passing the trigger logic and one of low transverse momentum failing the trigger logic. The position of the seed on the bottom sensor and the search window on the top sensor are shown in light-coloured strips. The distance between the mid-planes of the two sensors varies with the position in the tracker volume and ranges from 1.6 to 4.0 mm.

trigger logic, and is called a 'stub'. The window size for the coincidence can be programmed in the chip individually for each module to allow the adjustment of the p_T-threshold for different module positions and orientations throughout the entire tracker volume. The concept foresees the selection of tracks with $p_T \gtrsim 2\,\text{GeV/c}$. Programmable relative offsets are provided between the strips on both sensors to account for parallax corrections across the module, or potential misalignments. Translational misalignment between the two sensors can be taken into account by a common offset for the full module. Similarly, the window size can be adjusted across the module to handle potential variations in the sensor spacing after construction. These programmable parameters will be calibrated on real data following installation. Angular misalignment however would degrade the p_T resolution, as the effective p_T threshold for non-parallel strips would depend on the position of the particle passage along the strips; this poses strict demands on the assembly precision of the two sensors in a module. To keep the contribution of the angular misalignment to the p_T resolution negligible in comparison to the intrinsic resolution, the relative tilt between strips on both sensors should be significantly smaller than the strip pitch. In the case of the 2S-p_T module the deviation from parallel strips should be below 20 µm over the full length of the module. This corresponds to a 0.4 mrad tilt angle.

Figure 2 shows a conceptual picture of a 2S-p_T module. Signals from both sensor layers are fed to the CBC readout chips, which are bump-bonded onto one side of a flexible readout hybrid implemented in a technology that provides the necessary high density interconnectivity. The hybrid is folded around a stiffener and wire-bonded to both the top and the bottom sensor. The CBC chips perform the correlation operation required to identify high-p_T tracks, passing the stub information to the concentrator and controller circuits, called Concentrator Integrated Circuits (CIC) [4], which assemble the trigger data into a packet for transmission off-detector via the Low-Power Giga-Bit Transceiver (LP-GBT) [10] and Versatile Optical Link interface (VTRx+) [11]. The module also includes DC-DC power conversion components [12] to provide the low voltage supplies to the chips from a higher voltage supply rail. This makes the module a fully integrated entity, i.e. no additional adapter circuits are needed for operation.

2018 JINST 13 P03003

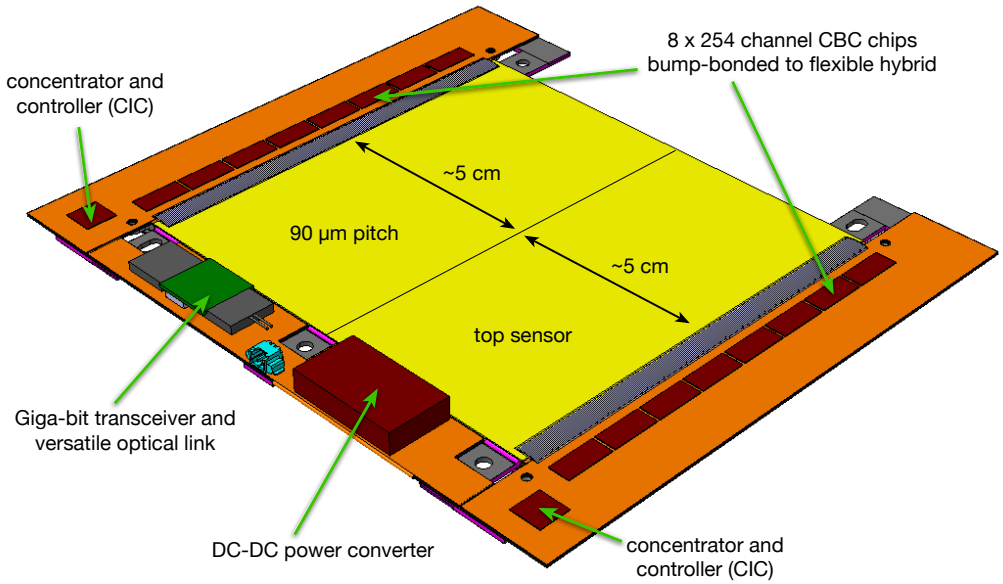

Figure 2. Conceptual view of the 2S-p_T module containing all electronic components. The sensors are planned to have an area of about $10 \times 10\,\mathrm{cm}^2$ with strips of about 5 cm length arranged in two rows (only the top sensor can be seen). The strip pitch is 90 µm. The two rows are read out from opposite ends via 2 x 8 CBCs, bump bonded onto the top surface of the hybrid. The hybrid is folded around a stiffener and wire-bonded to both the top and the bottom sensor, bringing the signals from each sensor to the CBCs for amplification and correlation.

Since each 2S-p_T module acts as an independent element in the tracker, correlation cannot be performed across module boundaries. To ensure hermetic coverage, modules on a given barrel layer or end-cap disk must overlap sufficiently so that a high-p_T track can be identified in at least one of the modules it intersects. For a barrel layer this implies placing modules at four different radii about a nominal radius, to enable the staggering of modules along z and ϕ. Additionally, the two halves of the p_T module are read out independently and as such would normally contribute to a stub finding inefficiency for severely inclined tracks. This effect becomes non-negligible for the innermost barrel layers of the tracker where the PS-p_T modules are located. However by progressively tilting the modules, along the length of the barrel, towards the interaction point, this geometrical loss can be recovered and hermetic coverage retained. Details of the Phase-II tracker layout and design can be found in [4].

2.2 The CBC2 chip

The CBC2 is a 130 nm CMOS chip designed for coarse pitch bump-bonding with a bond pitch of 250 µm. Figure 3 shows a block diagram of its internal architecture. The CBC2 does not yet contain all features planned for the future CMS tracker, but the general concept is fully established, with the main features described in what follows. A detailed description of the CBC2 and its functionality can be found elsewhere [13, 14].

2018 JINST 13 P03003

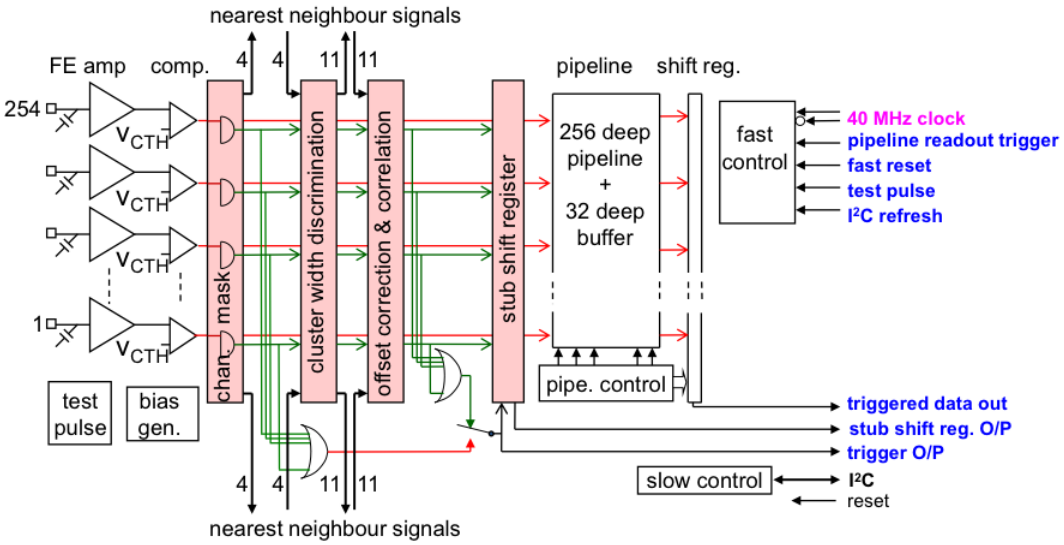

Figure 3. Block diagram of the CBC2 internal architecture. The relevant aspects for this beam test are explained in the text, more information can be found in ref. [13].

Each CBC2 has 254 readout channels to allow correlations between two sets of 127 sensor channels. Addresses are assigned to the strips according to their geometrical order on the sensors. Each channel has an amplifier followed by a comparator with a global comparator threshold voltage (V_{CTH}) and individually trimmed offset. If the signal charge on a channel exceeds the threshold, it is called a 'hit'. The comparator feeds two independent data flows, the high-p_T stub finding logic generating the input for L1, and the pipeline that buffers the data for subsequent triggered readout.

In the pipeline data flow, the outputs are sampled into the pipeline memory at 40 MHz, which corresponds to the frequency of the LHC clock. The full hit information is available for offline analysis from events that are accepted by L1.

In the trigger data flow, several steps are needed to construct 'online stubs', which are the input for L1. To suppress noisy channels, masking of individual channels is integrated without affecting the pipeline data flow. After masking, 'clusters' are formed in each sensor layer from adjacent hits to obtain the trajectory positions from both sensors. Wide clusters cannot be consistent with high-p_T tracks. The cluster width discrimination logic (CWD) selects only clusters of a given maximum width, which is programmable to be up to three strips. The cluster position is then assigned to the central strip; for a two-strip cluster, the center is defined as the strip with the lower address. The clusters are then used in the offset correction and correlation logic: a prompt trigger pulse is produced if a seed cluster in the bottom sensor is found to be in coincidence with a cluster occurring within a window in the top sensor. The window width is programmable with a maximum size of ±8 strips. The offset between the two sensors used to obtain a similar p_T-threshold over the full module is programmable independently for groups of 32 strips in steps of one, two, or three strips, providing enough tolerance to account also for translational misalignment by a common offset for the full module. The online stub position is given as the position of the cluster on the bottom sensor.

To avoid inefficiencies at the edges between two chips, i.e. when hits on bottom and top sensors are registered on different chips, inter-chip sharing of hit data is included for the four edge strips

2018 JINST 13 P03003

Table 1. Parameters of the silicon sensors of the two prototype 2S-p_T mini-modules operated in the beam test.

Manufacturer	Substrate	Thickness	Strip pitch	Strip length	Number of strips
Infineon	n-type	300 µm	80 µm	50 mm	256
CNM	p-type	270 µm	90 µm	54 mm	254

at each neighboring chip in the CWD, and of cluster data in the correlation logic for the 11 edge strips, as window size and offset can sum up to a maximum of 11.

The stub logic implemented in the CBC2 does not include the circuitry required to send the full list of stub positions and sizes. Instead, a single bit is set whenever at least one stub is found in the whole chip. Hence analysis of the stub data relied on offline emulation of the trigger logic.

The CBC2 is designed to accommodate both signal polarities, i.e. silicon sensors with n-type substrate as well as p-type substrate. The threshold value V_{CTH} acts oppositely for the different substrate types. For a p-type (n-type) sensor an increase of V_{CTH} lowers (increases) the signal threshold.

2.3 Prototype mini-modules

Two prototype 2S-p_T modules, named mini-modules, were operated simultaneously in the test beam, using two different sensor types from different manufacturers, with the features listed in table 1. Each module is constructed using two small sensors with either 254 (CNM[1]) or 256 (Infineon[2]) strips. Compared to the final module concept described in section 2.1, where each module constitutes a self-contained and independent unit, several components are replaced by custom pieces, as the final ones were still under development at the time of performing the experiments of this study. In particular, the final flexible hybrid was not available, so a custom prototype readout hybrid is used instead, called '2CBC2 hybrid'. The 2CBC2 hybrid is a small double-sided rigid hybrid on which two CBC2 chips are bump-bonded; details of the technology and design can be found in ref. [15]. Furthermore, these modules do not contain the CIC, LP-GBT, VTRx+ and DC-DC power conversion components; external components were used instead, as described in sections 2.4 and 3.1.

The sensors are wire-bonded to the 2CBC2 hybrid. While providing fewer channels compared to the full-size module, the strip length of these mini-modules is the same as in full-size modules (i.e. about 5 cm). The mid-planes of the sensors on a module are nominally separated by a distance of $d = 2.75\,mm$. Laboratory tests of the two mini-modules showed that the module with the Infineon sensors has several noisy and disconnected channels, while the module with the CNM sensors does not show any nonfunctional channels. For this reason, the module with CNM sensors was chosen as the device under test (DUT), while the other module served as a reference (REF). Figure 4 (left) shows a picture of the REF mini-module.

2.4 Beam test module construction

The mini-modules are assembled into identical units as shown in figure 4 (right). The 2S-p_T module is mounted on Peltier elements to stabilize the temperature of the hybrid at +20 °C throughout the test. The module is controlled by means of the so-called '2CBC2 interface board', which is a custom prototype development. The 2CBC2 interface board provides an electrical interface to the 2CBC2

[1]Institute of Microelectronics of Barcelona - Centro Nacional de Microelectrónica IMB-CNM. http://www.imb-cnm.csic.es.

[2]http://www.infineon.com.

2018 JINST 13 P03003

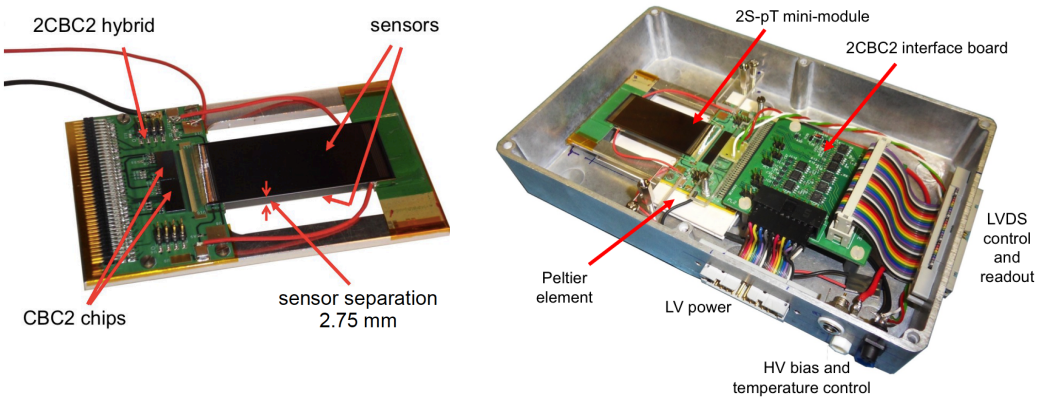

Figure 4. The prototype 2S-p_T mini-module with Infineon sensors (left) and the aluminium box with a mini-module and electronics (right) used in the test beam.

hybrid, supplying power and adapting signals to LVDS standard levels for transmission over the relatively long distances to and from the test beam data acquisition (DAQ) system.

3 Experimental setup

The setup was installed in area TB21 of the DESY-II test beam facility [16] in November 2013 for six days of data taking, using a positron beam. A schematic drawing including the sensor notations, S0 to S3, and the coordinate system is shown in figure 5. The DUT unit was mounted on a rotation stage, which in turn was mounted on yz-stages. The REF unit was fixed downstream. For both modules, the strips were oriented along the z-axis, which was also the rotation axis of the DUT. The rotation angle α is defined as the angle between the beam direction and a line normal to the DUT. The distance between the units, defined between the two module mid-planes, was about $L = 230\,\text{mm}$. In order to test the intrinsic efficiency of the CBC2 trigger logic, the online stubs were not used in the trigger decision. The trigger was provided externally by a coincidence between two scintillators, having an active area of about $2\,\text{cm}^2$.

The clock of the test beam accelerator runs at a frequency of 1.024 MHz, with a phase re-synchronisation to the 50 Hz of the power grid every 80 ms. The clock provided to the modules, however, is adapted to the LHC clock scheme. The LHC has a 40 MHz time structure and the CMS tracker readout runs synchronously. The fact that the two clocks were asynchronous needed to be considered in the DAQ design as well as in the data analysis. This caused the signal sampling of the module, which occurred at fixed phases of the LHC clock, to yield a slightly different fraction of the signal charge for each event, but the impact on the analysis was small, as will be shown in section 4.4.

3.1 Data acquisition

The DAQ system is illustrated in figure 6. Signals from the two scintillators were discriminated by the Trigger Logic Unit (TLU) [17] and a coincidence trigger was distributed to both the module DAQ and a fixed tracking telescope system (the DATURA telescope [18]), both installed in TB21. Due to time constraints no synchronisation of the two systems was carried out. Thus, no information from the telescope is used in the following analysis and it is not further discussed.

2018 JINST 13 P03003

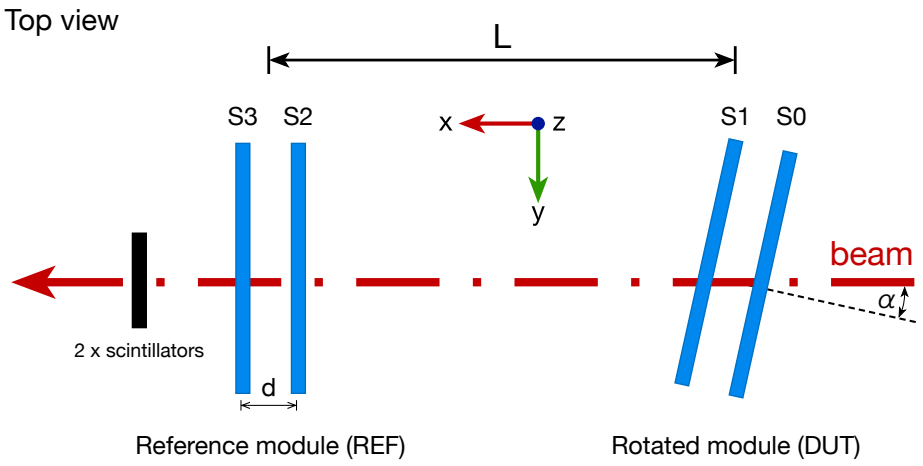

Figure 5. Schematic drawing of the test beam setup viewed from the top, showing the top (S0) and the bottom (S1) sensors of the DUT, and the top (S2) and bottom (S3) sensors of the REF. The beam direction is from right to left, traversing two scintillators on the downstream side of the two mini-modules. The x-y-plane of the coordinate system is horizontal, the z-axis is vertical.

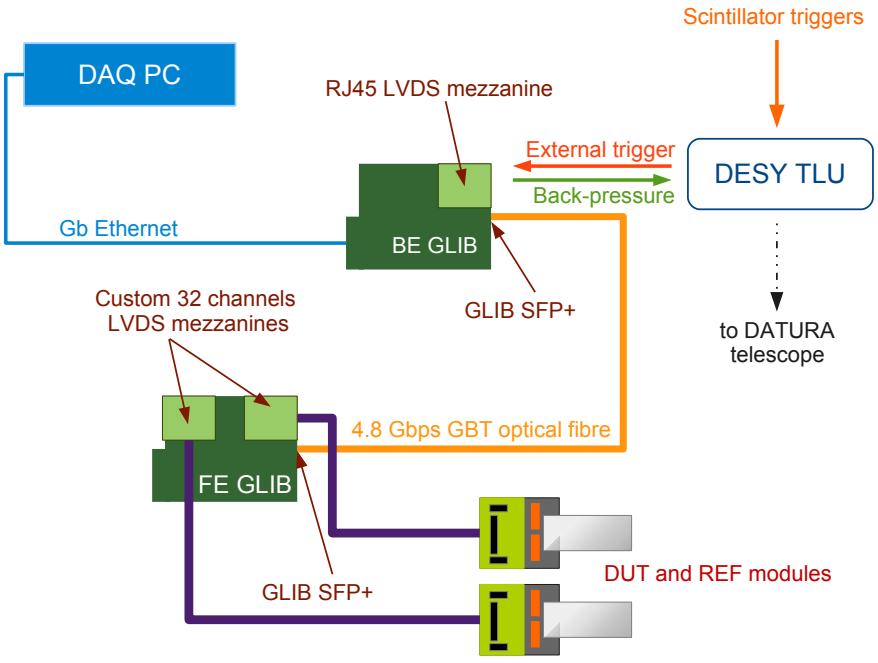

Figure 6. Diagram of the electronics setup as used in the test beam for data acquisition.

2018 JINST 13 P03003

The module DAQ was based on the CERN Gigabit Link Interface Board (GLIB) [19], a customisable electronics card for data acquisition and evaluation purposes, based on the Xilinx Virtex 6 FPGA.[3] The card can be configured to interface with a range of external hardware via two on-board mezzanine headers, and can host up to four SFP+ transceiver modules for optical data transmission.

The prototype mini-module DAQ system emulated the architecture that is being considered for readout and control of full-size 2S modules: a front-end (FE) GLIB was configured to interface with the two mini-modules, fulfilling the role of the CIC and LP-GBT ASICs that will eventually be employed in the final system; and a back-end (BE) GLIB was configured to communicate with the FE board while implementing the logic needed for controlling the CBC2s, buffering and packaging the returning data streams and transmitting the event payload to a PC farm. As is envisaged in the final system, communication between the BE and FE was achieved via a single optical fibre for long distance transmission at 4.8 Gbps using the GBT protocol. This provided a bidirectional data transmission channel for readout and control with 3.28 Gbps usable bandwidth in each direction.

The BE board also interfaced to the TLU, receiving the asynchronous trigger described above and providing it with a return LVDS back pressure signal. The TLU was configured to throttle the scintillator trigger when back pressure was detected. In this way the BE board was used to prevent data buffer overflows in the DAQ system, but also to pause data taking during a run, or stop at the end of a run.

The BE GLIB measured the arrival time of the asynchronous trigger from the TLU with respect to the internal 40 MHz system clock used to run the entire DAQ system. By splitting the 40 MHz clock into eight time buckets, a Time to Digital Converter (TDC) block implemented in firmware on the BE board recorded the trigger arrival time with respect to the system clock to within 3.125 ns.

Like the hardware, the software has been designed to be as compatible as possible with the standard CMS run control software. The processes were based on a common C++ development framework, XDAQ [20]. The complete run control software chain was composed of standard CMS software components tuned to fit the specific needs of this test beam architecture. Synchronisation between all software components was ensured by a Run Control and Monitoring System (RCMS) process [21]. This top-level application was used as a centralized access point to the DAQ framework in order to configure the system, to start data taking, and to stop or pause the data acquisition process.

3.2 Calibration tasks

Each CBC2 front end amplifier output is DC-coupled to a comparator (Figure 3). A single global comparator threshold (V_{CTH}) is implemented for the CBC2, which applies to all channels on the chip. Naturally occurring manufacturing variations result in small differences (offsets) amongst the DC levels of the amplifier outputs, which must be corrected for to ensure uniform sensitivity to input signals for all channels. Each channel is therefore provided with a programmable offset register that can be used to trim the amplifier DC output levels, as detailed in ref. [8, 22]. An iterative trimming procedure was used to adjust the DC levels of the pedestals (the level when no signal is present) by varying V_{CTH} to find the point where the channel comparators fired 50% of the

[3] VLX130T-1FFG1156C, https://www.xilinx.com/support/documentation/data_sheets/ds150.pdf.

2018 JINST 13 P03003

time, then adjusting each of the offset correction bits, one at a time, depending on whether the 50% V_{CTH} value was above or below the target V_{CTH} pedestal value.

To save time, offset tuning was performed in the laboratory, saving the values in a file that could be quickly programmed into the chips in the test beam setup. It was then sufficient to program V_{CTH} to investigate the response of the chip to beam particles for a particular global threshold setting.

The latency for each of the two data flows also required adjustment, called data latency (for pipeline data flow) and stub latency (for trigger data flow). The data latency is the delay, in 25 ns clock intervals, between the storage of the hit data for every event in the CBC2 pipeline and the arrival of a trigger; it is a parameter intrinsic to the CBC2 that requires adjustment. The comparator outputs are clocked into the CBC2 pipeline every 25 ns clock cycle. The pipeline provides the data storage necessary to allow the GLIB to receive, process and transmit the trigger generated by the TLU. The GLIB triggers the readout of the CBC2 pipeline at a fixed time with respect to the TLU trigger, so the data latency parameter in the CBC2 must be appropriately programmed to ensure that the correct data are retrieved from the pipeline.

The stub latency is the delay between the arrival of the trigger from the TLU and the stub bits at the GLIB; it defines which stub bits relevant to a specific event should be read out from the GLIB memory. This is therefore a GLIB parameter specific to the test beam setup.

3.3 Recorded data sets

For each event triggered by the TLU the information from both streams was stored: the incidence of a stub trigger from a CBC2, along with the full hit information from the event that generated the trigger. From the REF, only the data stream was used, while from the DUT data and stubs were relevant for offline analysis. The trigger logic of the stubs was configured by setting the CWD to three strips, the window width to ± 7 strips and the offset to zero strips. Each time a cluster was found on S1, a window was seeded to find a correlation on S0.

Several commissioning runs were performed to choose optimal settings of all relevant calibration parameters. The commissioning data comprise dedicated runs for latency scans of both output streams (i.e. stubs for the trigger path, and the triggered data) as well as threshold scans of V_{CTH} for both modules. Also randomly triggered events without beam were recorded for noise studies. After commissioning, events were recorded for offline analysis using the optimised settings, changing only the DUT configuration. Analysis runs included V_{CTH} scans of the DUT and angular scans using different settings of the rotation stage. The beam energy was changed only during the commissioning phase and then kept constant at 4 GeV.

Data were taken for each run with a fixed configuration. The typical run size was about 500, 000 triggered events, leading to negligible statistical uncertainties in the offline analysis. To measure the low noise level, the run size without beam was about one million randomly triggered events.

4 Event reconstruction

Following commissioning and calibration, events needed to be reconstructed for offline analysis. First, noisy strips were identified and excluded, so clustering and stub reconstruction could be carried out and event selection could be performed. The alignment of the system was then determined.

2018 JINST 13 P03003

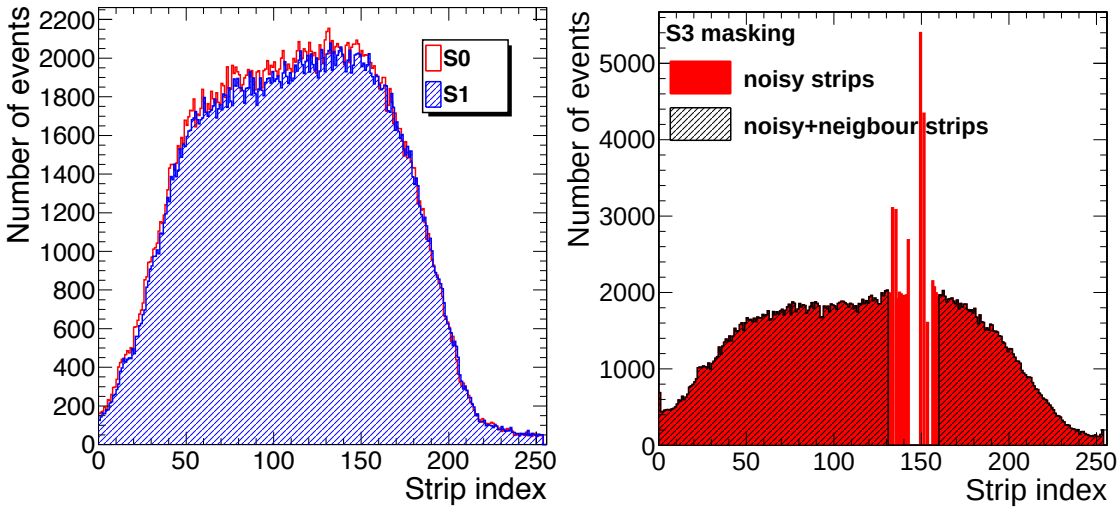

Figure 7. Number of hits per strip in events with beam from analysis runs after full calibration for the two DUT sensors S0 and S1 (left). The beam profile on the sensor S3 of the REF (right) is shown in red after masking the noisy strips (strips with zero events), but not their neighboring strips, and in black after masking both, the noisy strips and their neighboring strips.

4.1 Noise suppression

The first step was an estimation of the intrinsic noise in the modules using randomly triggered events without beam. This step revealed two kinds of electronic noise.

The main noise source concerned a limited number of very noisy channels on both sensors of the REF, S2 and S3. As a result, the corresponding channels generated hits in up to 70% of randomly triggered events. The affected strips were masked, by raising the offset values of the comparators for the later commissioning and analysis runs. A small number of noisy strips was expected from leakage current variations that occur as a result of the sensor manufacturing process.

After masking, an analysis of randomly triggered events suggests that the number of hits per event follows a binomial distribution if strips are independent. Furthermore, with the optimal thresholds used during the beam test (section 4.5), the probability of a strip randomly firing is of the order of 10^{-7}.

The hit distributions in the sensors in events with beam (Figure 7 (right)) revealed that channels adjacent to noisy channels were also slightly affected by noise, which could only be seen after full calibration. However all problematic channels for sensors S2 and S3 of the REF were in the same region of size about 30 strips, and this region could be easily masked for the analysis. The study also confirmed that the DUT required no masking, as can be seen in figure 7 (left). The beam profile reflected in these distributions shows that the modules were well centered around the scintillators and the beam.

4.2 Offline reconstruction

As the CBC2 chips generated clusters and stubs, similar definitions were chosen for the analysis of the offline data. However to obtain maximum precision, their positions were calculated by averaging

2018 JINST 13 P03003

as explained in the following. The definitions are all in units of strips, and are only converted to lengths where needed.

As the signal information is binary, a group of adjacent hits is considered a cluster. The cluster width w is defined as the number of strips in the cluster

$$w = n_{\text{last}} - n_{\text{first}} + 1\,, \tag{4.1}$$

where n_{first} and n_{last} are the indices of the first and last strips in the cluster, respectively, in accordance with the geometric order of the strips on the sensors. This quantity corresponds to the CWD size used in the trigger stream. The cluster position X is defined as the mean value

$$X = \frac{n_{\text{first}} + n_{\text{last}}}{2}\,. \tag{4.2}$$

The cluster width is given in steps of full-strips, while the position is in half-strips.

Stubs were reconstructed from the pipeline stream and referred to as 'offline stubs'. The stub position μ is defined as the mean cluster position per module

$$\mu = \frac{X_{\text{top}} + X_{\text{bottom}}}{2}\,, \tag{4.3}$$

where X_{top} and X_{bottom} are the cluster positions in the top and bottom sensor of the module, respectively. The stub direction ΔX is defined as the difference between the cluster positions in the top and bottom sensor,

$$\Delta X = X_{\text{top}} - X_{\text{bottom}}\,. \tag{4.4}$$

The stub direction ΔX corresponds to the quantity used to define online stubs in the trigger stream where it is given in steps of full-strips, i.e. a trigger was generated if ΔX was within the configured window size, but as already mentioned has a finer granularity for offline stubs: the stub direction is given in steps of half-strips, while the stub position is in quarter-strips.

For several of the following studies it is essential to select events where exactly one positron passed through all four sensors with high probability. Such events are selected by requiring exactly one cluster on each of the four sensors, and are called 'clean events'.

4.3 Latency adjustment

As explained in section 3.2, data and stub latencies had to be properly set prior to data taking. The data latency was optimised by maximising the number of hits in the sensors. Figure 8 (left) indicates that the best value is 17, corresponding to a latency of $17 \cdot 25\,\text{ns} = 425\,\text{ns}$. A large number of events is also seen in the neighboring pipeline cells, which was caused by the asynchronous clock. The value is in good agreement with the delay expected from the cable length, which was used to define the scanning range from 14 to 18.

For a given data latency value, the stub latency could be chosen by comparing offline and online stubs. This was the only study where offline stubs were not reconstructed as described in section 4.2 but exactly as the online stubs, to allow a direct comparison. An offline stub is called 'emulated' if it fulfills the online stub criterion, i.e. when $\Delta X \leq 7$. The optimal stub latency is found to be 12 based on a maximum in the fraction of events with online and emulated stubs (figure 8 (right)). This plot also illustrates that the stub logic in the CBC2 worked as expected, i.e. with a perfect

2018 JINST 13 P03003

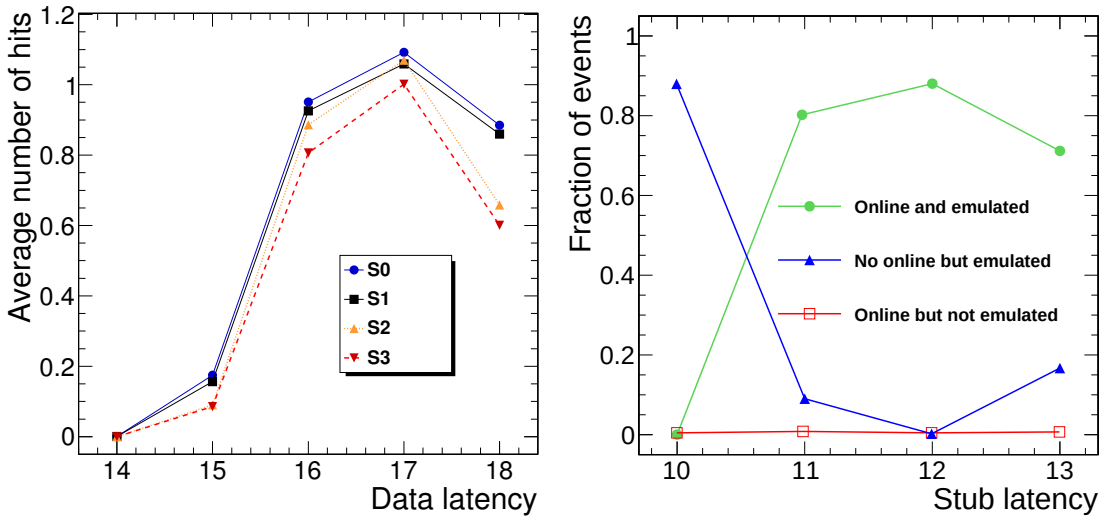

Figure 8. Average number of hits per event for each sensor at different values of the data latency (left). Fraction of events having an online stub and/or an emulated stub on the DUT at different values of the stub latency, for the optimized data latency value of 17 (right). Both distributions are in units of 25 ns LHC clock intervals.

match between online stub and emulated stub. Stubs were not found in each triggered event; the maximum fraction of events containing stubs reaches a value around 90%. This is mainly due to particles that missed the active area of at least one of the DUT sensors, and some small effects such as fake triggers, clusters wider than three strips that failed the CWD criterion, or inefficiencies of the sensors. The values of 17 and 12 for data and stub latency, respectively, were used for all further analysis.

4.4 TDC phase

As discussed in section 3.1, a TDC was used to measure the phase difference between the positron passage and the time of the event sampling, by splitting the LHC clock into eight intervals corresponding to 3.125 ns each. The hit efficiency of the sensors was used to study the dependence of the performance on the TDC phase, and is defined as follows. Using clean events, the stub direction could be fitted by a Gaussian function. The mean and width (σ) resulting from this fit are used to define a window that starts from a cluster found on the first sensor and contains all the expected clusters on the other sensor within $\pm 5\sigma$ of the mean predicted position. Finally, for a given sensor, using events with one cluster on each of the three other sensors, the efficiency was defined as the fraction of events with a hit in the expected window.

Figure 9 shows the efficiency of the DUT sensor S0 as a function of the TDC phase for different V_{CTH} values. As mentioned in section 2.2, the CBC2 supports either n-type and p-type sensor substrates, but the behaviour of the threshold value V_{CTH} depends on the substrate type. Since the DUT has p-type sensors an increase of V_{CTH} lowers the signal threshold. For the optimised value of $V_{\mathrm{CTH}} = 120$ (section 4.5), corresponding to a low threshold, the efficiency does not depend on the TDC phase, which is relevant, as modules will be placed at very different positions throughout the outer tracker volume, and time-of-flight differences will occur for traversing charged particles.

2018 JINST 13 P03003

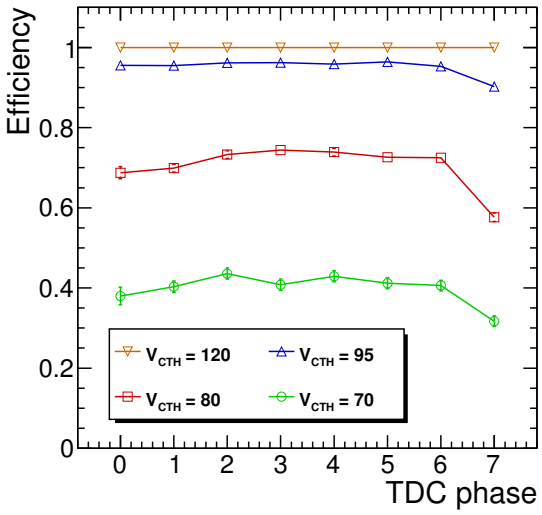

Figure 9. Sensor hit efficiency of DUT sensor S0 as a function of the TDC phase, in units of 3.125 ns, for different values of V_{CTH}.

Nevertheless, corrections need to be made for time-of-flight effects in the current and in the future tracker to mitigate signals from out-of-time pileup, i.e. signals from the previous and following bunch crossings. For values of V_{CTH} corresponding to high thresholds, much higher than would be used in detector operation, the overall efficiency decreases as expected. For these high thresholds, the efficiency is constant for intermediate values of the TDC phase, but drops for extreme values.

4.5 Threshold determination

Since the DUT is a module with p-type sensors (the REF is a module with n-type sensors) an increase of V_{CTH} lowers (increases) the signal threshold. While tuning V_{CTH}, the main objective was to achieve a threshold that is sufficiently above the noise but allows maximum efficiency over a wide angular region that includes most high-p_T stubs. This would be the objective for operation in CMS.

During commissioning, the V_{CTH} values of all chips on both modules were scanned simultaneously to identify the level at which signals occurred due to noise, which was done by counting the average number of hits per event on the sensor at normal beam incidence, as shown in the left panel of figure 10. According to geometric expectations, passage of a particle within the active sensor area should create mainly one-strip clusters, and sometimes two-strip clusters. As discussed in section 4.3 there are reasons why some events have zero hits. Therefore, with appropriate threshold values the average number of hits is expected to be close to one. Noise appears approximately at $V_{\mathrm{CTH}} \gtrsim 125$ for the DUT, and for the REF at $V_{\mathrm{CTH}} \lesssim 145$. Both sensors of a module behave similarly.

The fraction of clean events and the average number of hits for the DUT are shown in the right panel of figure 10 in the range from $V_{\mathrm{CTH}} = 30$ (high threshold) to $V_{\mathrm{CTH}} = 120$ (low threshold), while the REF was kept at a fixed value of $V_{\mathrm{CTH}} = 150$. Towards low thresholds the fraction of clean events increases, and the average number of hits per sensor shows a normal behavior. This study was performed at normal beam incidence, but as the performance should be optimal also for

2018 JINST 13 P03003

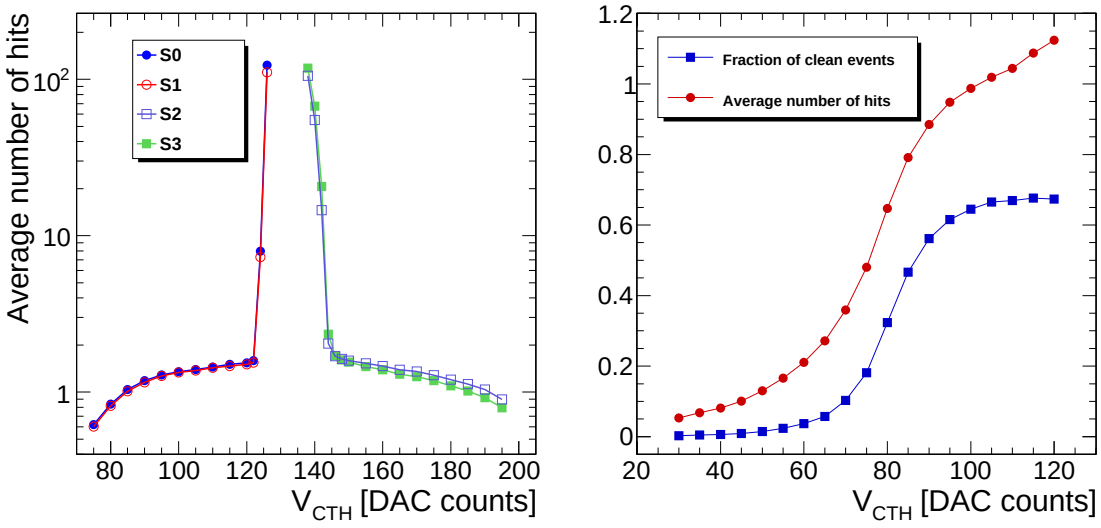

Figure 10. Average number of hits for all four sensors S0 to S3 as function of V_{CTH} from commissioning runs (left) and fraction of clean events and average number of hits for DUT sensor S0 as a function of V_{CTH} from analysis runs after full calibration (right).

different incident angles, values close to the noise onset should be chosen. The optimal value for the DUT is $V_{CTH} = 120$, and was used in the following, except in analyses using a scan of this parameter. The optimal value for the REF is found to be $V_{CTH} = 150$ using the same approach, and is kept constant for all following studies.

The maximum fraction of clean events is limited by several effects. The positrons did not always cross the active area of all sensors; there were tracks that missed some or all sensors, or lay within the masked region. In addition, as discussed earlier, the asynchronous beam meant an event might not always occur sufficiently in phase with the CBC2 clock. Small effects arose also from events with more than one positron, from interactions with the material, and from potential fake triggers. Noise or inefficiencies of the sensors caused minimal effects. For electron or positron beams, the critical energy at which radiative losses exceed ionisation losses in silicon is about 40 MeV [23], so a significant background of extra hits is expected in the sensors for a 4 GeV/c beam. The fraction of clean events is thus a measure of the fraction of events where exactly one positron passed through the analysed area of all four sensors in time with the CBC2 clock.

As the CBC2 amplifiers have slightly different gains, the two chips on a module were not expected to be identical in terms of actual V_{CTH} values. The approximate electron equivalents for different V_{CTH} values were obtained using chip-internal test pulses with different amplitudes. When averaging over all channels for one CBC2, one V_{CTH} step was found to correspond to about 360 electrons for the DUT chip CBC2-0, and to about 400 electrons for the DUT chip CBC2-1, with 10% uncertainty. Due to the individual offset corrections of all channels described in section 3.2, the charge equivalents are similar for low thresholds, e.g. for the optimised value of $V_{CTH} = 120$ there were around 6500 electrons for both DUT chips. At higher thresholds, the difference in the charge equivalents between the DUT chips increases, e.g. for the highest analysed threshold of $V_{CTH} = 30$, the charge equivalents are about 39000 electrons for CBC2-0 and 43000 electrons for CBC2-1.

2018 JINST 13 P03003

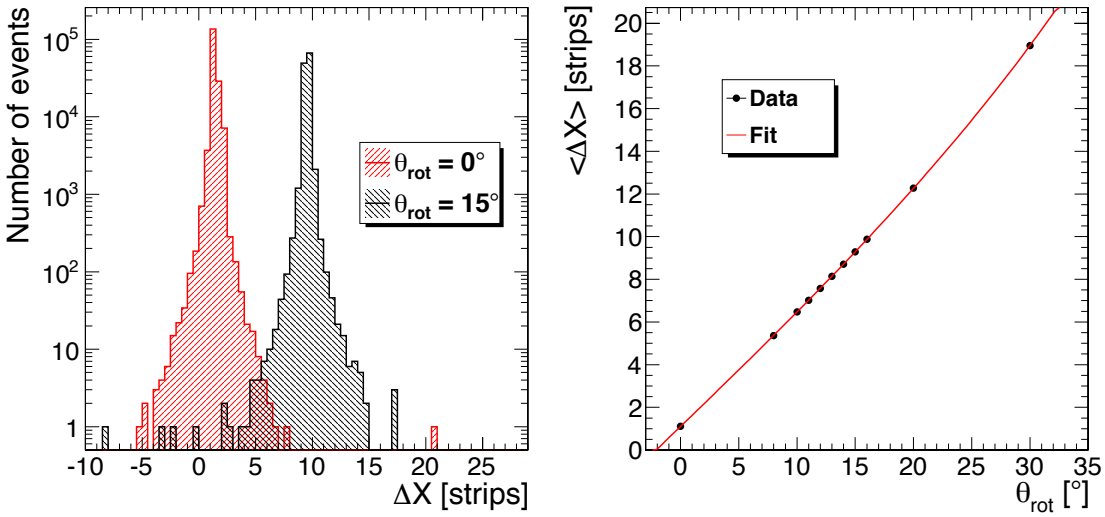

Figure 11. Distribution of the stub direction of the DUT in clean events, with the additional requirement that the stub direction of the REF is within ±4 strips, for two different angles of the rotation stage (left), and mean stub direction as a function of the angle of the rotation stage including the fit (right).

4.6 Alignment of the DUT

The last step in the calibration process was to determine the alignment between the setup and the beam. Using the rotation stage, the angle α of the DUT could be adjusted as illustrated in figure 5, where α was the angle between the beam direction and a line normal to the DUT, with the rotation axis parallel to the strips. This angle corresponded to the angle θ_{rot} as read from the rotation stage, but might have an angular offset θ_0 between the beam and the normal to the module at $\theta_{\text{rot}} = 0$, so it is given by $\alpha = \theta_{\text{rot}} + \theta_0$. The dependence of the stub direction ΔX on θ_{rot}, as seen in figure 11 (left), was used to extract information about the alignment.

If θ_{rot} and θ_0 are the angles described above, d is the distance between the two sensors, $p = 90\,\mu\text{m}$ the strip pitch, and ΔX_0 the translational misalignment of the two sensors, the stub direction ΔX can be written as

$$\Delta X = \Delta X_0 + \frac{d}{p} \tan(\theta_{\text{rot}} + \theta_0)\,. \tag{4.5}$$

This function was used to fit the data as shown in figure 11 (right). The resulting parameters are $\Delta X_0 = -0.03 \pm 0.05$ strips, $d = 2.72 \pm 0.01$ mm and $\theta_0 = 2.1° \pm 0.1°$.

The values are compatible with good alignment between the two sensors and the value is set to $\Delta X_0 = 0$. For the sensor spacing the deviation from the nominal value of 2.75 mm is small, and $d = 2.72$ mm is used later. The beam incident angle α needs to be corrected by the estimated offset. A repetition of the fit while fixing the sensor misalignment to $\Delta X_0 = 0$ leads to a slightly smaller angle — therefore it is set in the following to $\alpha = \theta_{\text{rot}} + 2°$.

5 Beam parameters

A measurement of the beam divergence was necessary to obtain the increase in beam diameter as beam particles traversed the setup. Also, a possible misalignment of the two modules with respect to

2018 JINST 13 P03003

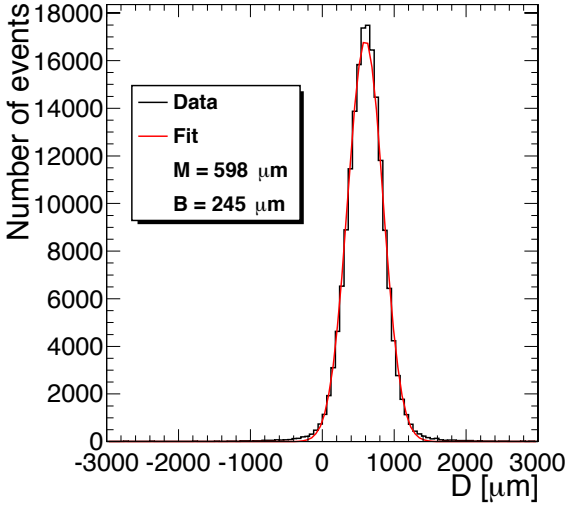

Figure 12. Distribution of the difference of stub positions between the two modules in clean events, transformed to lengths using the strip pitches. Also shown is the Gaussian fit and the fit results of the mean value M and the standard deviation B.

the beam axis needed to be quantified. Both quantities could be obtained from a single distribution using clean events only, calculating the difference between the offline stub positions. However, as the strip pitch of each module was different, the stub difference D was calculated as the difference of the stub positions μ, transformed to lengths using the strip pitches p, as

$$D = \mu_{\mathrm{DUT}} \times p_{\mathrm{DUT}} - \mu_{\mathrm{REF}} \times p_{\mathrm{REF}} \,. \tag{5.1}$$

The corresponding distribution is shown in figure 12, together with the Gaussian fit performed. The mean of the fit corresponds to the misalignment of the two modules of $M = 598\,\mu\mathrm{m}$, while the width reflects the beam divergence with a standard deviation of $B = 245\,\mu\mathrm{m}$. Knowing the distance L between the two modules, the angular measurement Θ of the beam divergence could be calculated from $\tan(\Theta) = B/L$, resulting in 1.06 mrad. This value is in agreement with DESY-II beam specifications of about 1 mrad.

The beam divergence was used to make track predictions from one module to the other. After correcting for the misalignment by the mean value, a cluster from a positron passage through one module that is found within the region of $\pm$ FWHM $\approx \pm 575\,\mu\mathrm{m}$ around the stub position in the other module was considered to be consistent within the beam divergence. This choice was motivated by the fact that in this region the distribution showed almost perfect Gaussian behaviour, while outside this range the tails deviated from the fit. This was taken into account in the analysis where needed.

6 Results

Using data from dedicated analysis runs following calibration and commissioning, studies of the module performance were carried out to establish the behaviour of the cluster parameters, cluster efficiencies and the efficiency of the stub trigger logic. The parameters varied were V_{CTH} and the

2018 JINST 13 P03003

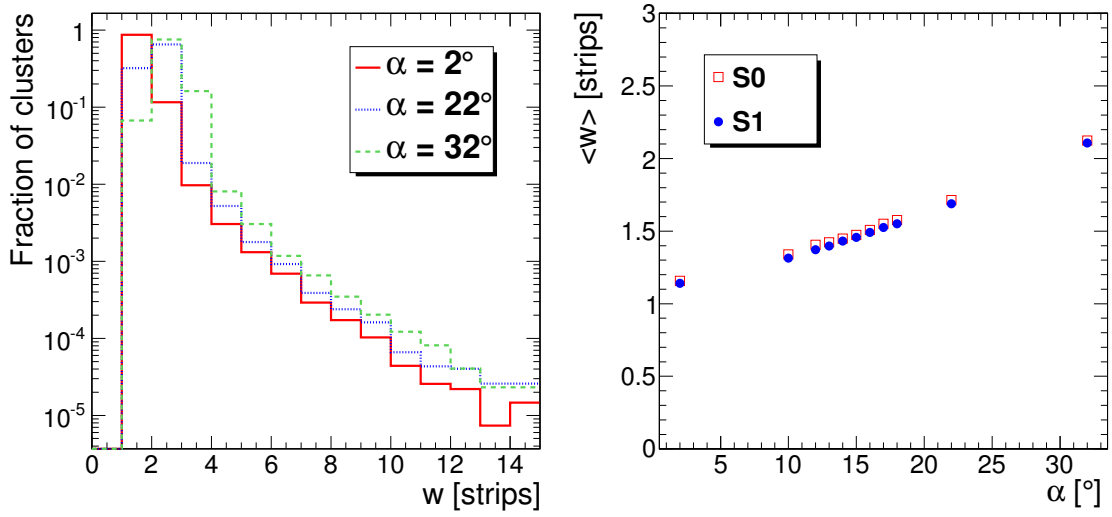

Figure 13. Normalised cluster width distributions for different incident angles on the DUT sensor S0 (left). Mean cluster widths as a function of the beam incident angle for the sensors S0 and S1 of the DUT (right).

rotation angle of the DUT, scanning both in suitable steps. If not stated otherwise, the results that follow were obtained for variations of either V_{CTH} or the beam incident angle α, keeping the other parameter at the optimised value of $V_{\mathrm{CTH}} = 120$ or $\alpha = 2°$.

6.1 Cluster width

The cluster width distributions of one of the DUT sensors at different incident angles are shown in the left panel of figure 13. In the right panel the mean values of the cluster width for the two sensors of the DUT as a function of the incident angle of the beam are shown. The expected broadening of the clusters for steeper angles with respect to the sensor's normal is visible, and the two sensors behave similarly. For all angles a long tail of large cluster widths is visible. This can be related to delta rays, and to radiative energy loss by positrons.

The fraction of clusters with different cluster widths is shown as a function of incident angle in figure 14. At $\alpha = 2°$, close to 90% are single-strip clusters, about 10% are two-strip clusters and approximately 1% are multi-strip clusters. The fraction of single-strip clusters decreases with increasing incident angle, and at around $\alpha = 16°$ this fraction is similar to that for two-strip clusters, which dominates for higher angles, reaching about 75% at 32°. A visible increase in three-strip clusters is observed between 22° and 32°, exceeding single-strip clusters at about 29 degrees. It should be noted that wide clusters, with a width above five strips, do not show a strong dependence on the incident angle. This supports the hypothesis of delta rays and radiative energy loss by positrons, for which the propagation in the silicon bulk is less dependent on the primary particle direction. In general, the choice of a value of three for CWD for the trigger stubs was reasonable for all angles, as this included more than 99% of the clusters.

The effect of V_{CTH} on the cluster width is shown in figure 15 (left). As already shown, the average cluster width for the optimised value of $V_{\mathrm{CTH}} = 120$ is slightly below 1.2 strips, and the distribution shows a long tail at higher values. For a high threshold of $V_{\mathrm{CTH}} = 70$, cluster sizes

2018 JINST 13 P03003

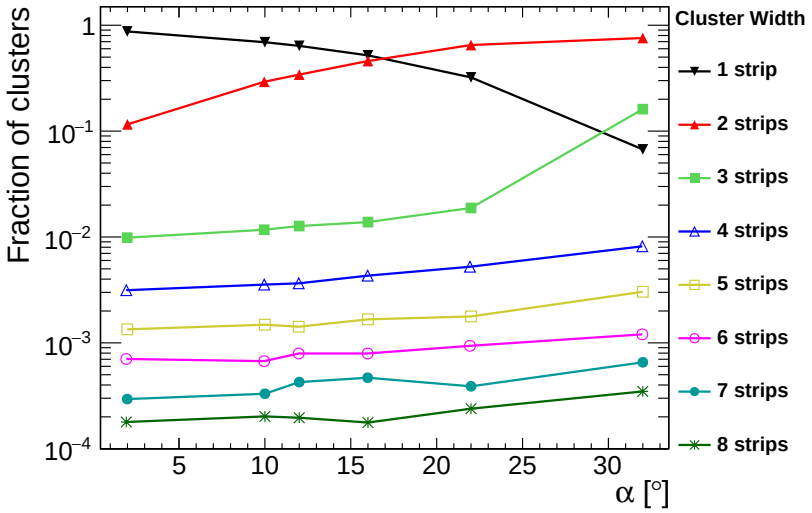

Figure 14. Fractions of clusters with different strip multiplicities shown as a function of incident angle for the DUT sensor S0.

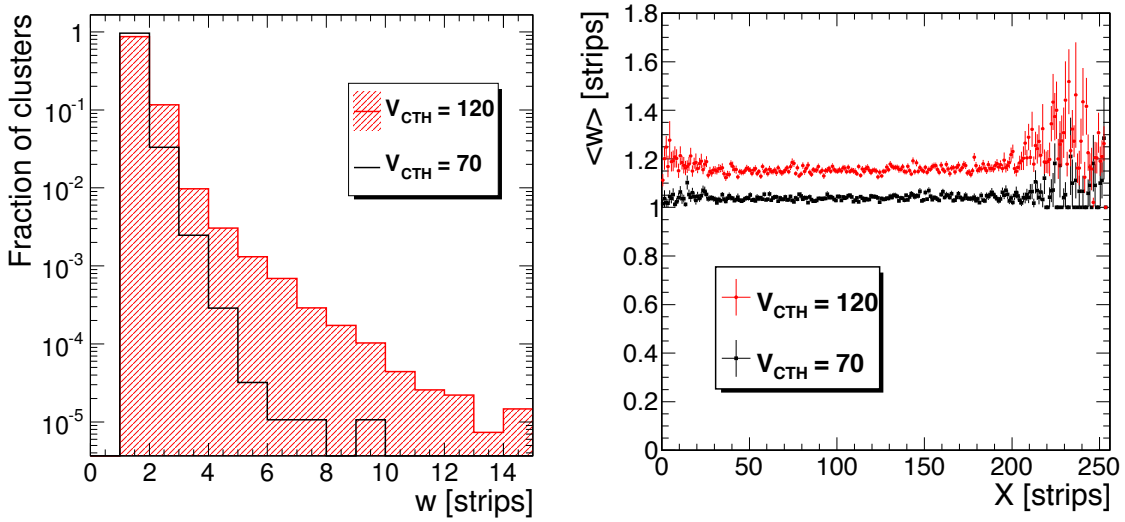

Figure 15. Normalised cluster width distribution (left) and mean cluster width as a function of the cluster position on the sensor (right) for two different values of V_{CTH} for the DUT sensor S0. The error bars show the statistical uncertainty.

larger than one are strongly suppressed. This was expected, as almost the full thickness needed to be ionised to still measure signals for such high thresholds. The mean cluster width is uniform throughout the detector independent of V_{CTH}, as can be seen in figure 15 (right).

6.2 Cluster efficiency

Due to the absence of telescope data, no track prediction could be obtained from an external device. Thus, in order to define a cluster efficiency, tracks were reconstructed using information from three

2018 JINST 13 P03003

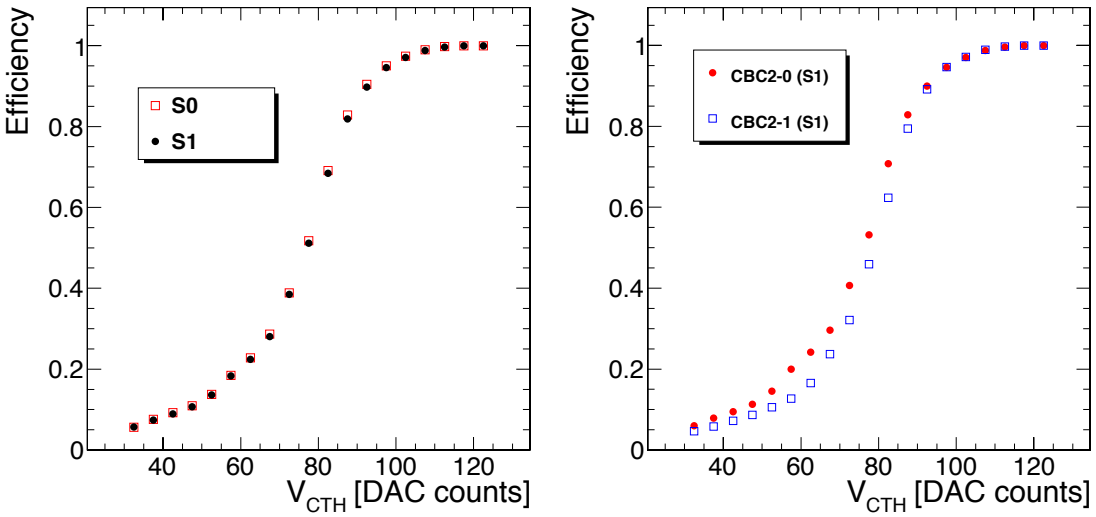

Figure 16. Cluster efficiency as function of V_{CTH}. Per-sensor efficiency for DUT sensors S0 and S1 (left). Per-chip efficiency for the two chips (CBC2-0 and CBC2-1) connected to S1 (right).

sensors, and extrapolated into the fourth sensor. Inefficiencies due to edge effects were avoided by excluding cases where the track prediction pointed to a masked region or outside the active area of the sensor under study. The efficiency was studied for the DUT; the REF was only used for the track prediction. To select events where exactly one positron passed through the analysed area of all four sensors with a high probability, the following criteria were applied for the three sensors not under study:

- exactly one cluster on each sensor,
- cluster positions X must be at least four strips away from the edges and from masked strips,
- for the REF, the offline stub direction must be $|\Delta X| \leq 4$ strips,
- for the DUT sensor not under study, the cluster position X must be within the beam divergence with respect to the REF offline stub position μ (section 5).

The above criteria defined the number of events for the denominator of the 'per-sensor efficiency'. Events entered the numerator if the DUT sensor under study had at least one cluster within a window of ±4 strips around the cluster on the other DUT sensor, i.e. the DUT offline stub direction fulfilled $|\Delta X| \leq 4$ strips.

The efficiency was measured for both DUT sensors at the optimal threshold of $V_{\mathrm{CTH}} = 120$, but was also studied as a function of threshold by varying the V_{CTH} value of both CBC2 chips of the DUT in steps of 5 in a range from 30 to 120 simultaneously, as shown in figure 16 (left). The value at optimal threshold is of importance to understand the module performance and to interpret the online stub trigger efficiency in section 6.3. Although thresholds much higher than the optimal value would not be used in real detector operation, it is important to see if this novel 2S-p_T module concept with a completely new chip functions according to expectations.

2018 JINST 13 P03003

For the statistical interpretation of the measured efficiency values one needs to take into account that the track prediction uses the cluster on the DUT sensor not under study, i.e. the cluster of the sensor not under study enters the denominator of the efficiency definition. The clusters on the two DUT sensors might be correlated, due to the fact that they are identical sensors and the V_{CTH} values used in the scans were identical since the two sensors were connected to the same chips. However, the correlation is expected to be small as the dominant contribution to the variation in charge collected should be the Landau fluctuations. If no correlation were present, the measured efficiency would correspond to the true efficiency. Thus, the measured efficiency is the upper limit, according to the given correlation.

To understand and quantify the deviation of this upper limit from the true efficiency, the per-sensor efficiency was cross-checked using the same definition of the denominator as in section 6.3, where only requirements on the REF were imposed, but no precise track prediction was available. The absolute efficiency values of S0 and S1 using this cross-check definition are smaller for all V_{CTH} values, as expected, but similar. For the lowest and highest thresholds analysed, the difference in efficiency between the two definitions is below 0.4%. The difference slightly increases for intermediate threshold values, and reaches a maximum of about 2.5% at $V_{\mathrm{CTH}} = 80$. For all values of $V_{\mathrm{CTH}} \geq 90$ the difference is below 1%. The cross-check definition was not used for the results in this section, but only to quantify the bias. The reported efficiencies are thus upper limits with systematic upwards biases of up to 2.5%.

Both DUT sensors behave similarly, as shown in figure 16 (left). The dependence on V_{CTH} reflects qualitatively the expectations based on the Landau distribution of induced charge; a perfect reflection of Landau distributions is not expected, due to charge sharing and binary readout. The per-sensor efficiency at the optimal threshold is consistent within statistical uncertainties for the two DUT sensors, and found to be above 99.5%, including the systematic uncertainty.

The efficiency was also studied in different sensor regions to search for variations between the two CBC2 chips on the module. This was achieved by only using hits on one half of the sensor, and requiring in addition that the cluster position of the sensor not under study was at least four strips away from the sensor center to exclude edge effects. Figure 16 (right) shows the per-chip efficiency as a function of V_{CTH} for the two CBC2s of DUT sensor S1. When comparing the two chips, one has a systematically higher efficiency for lower V_{CTH} values than the other. This behaviour is observed on both DUT sensors. This difference could also be verified by a characterisation of the chips using test pulses, estimating the electron equivalence for V_{CTH} as described in section 4.5. As explained earlier, small differences between chips are indeed expected from normal manufacturing variations, resulting in different electron equivalents for higher thresholds, and thus differences in efficiencies. The per-chip efficiency at the optimised V_{CTH} values was determined for both the DUT and the REF module. The values of the eight per-chip regions on the four sensors agree within statistical uncertainties, and are, like the per-sensor efficiencies, above 99.5%, including the systematic uncertainty.

A few dedicated runs were recorded where both V_{CTH} and incident angle were varied. This allowed us to measure the dependence of the efficiency on both parameters simultaneously, as shown in figure 17. The search window on the DUT sensor under study of ±4 strips needed to be shifted with respect to the cluster on the other DUT sensor by the mean stub direction (figure 11). In the same way, the search region of clusters on the DUT with respect to the offline stub position

2018 JINST 13 P03003

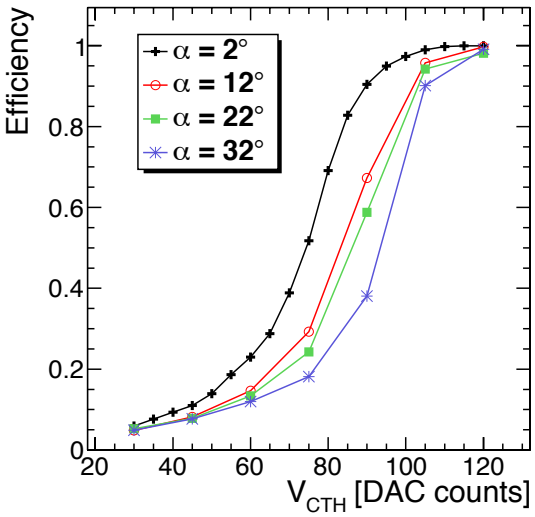

Figure 17. Per-sensor efficiency for DUT sensor S0 as function of V_{CTH}, for different incident angles α.

on the REF — which is related to the beam divergence — had to be adjusted, as this value varied with the rotation of the DUT. At the optimised value of $V_{\mathrm{CTH}} = 120$ the measured efficiencies are close to 100% and independent of the incident angle.

6.3 Stub efficiency

The correlation logic of the CBC2 has been tested by rotating the DUT, thus emulating the bending of tracks in the magnetic field. The beam incident angle α represents a particle with a certain bending radius in the transverse plane r_{T} for a given radial position of the module in the tracker R, following the equation $\sin(\alpha) = R/2r_{\mathrm{T}}$. This bending radius corresponds to a particle with certain charge q and transverse momentum p_T, for a homogeneous magnetic field of given strength B, via the relation $r_{\mathrm{T}} = p_T/qB$. For typical units, under the assumption of $q = \pm e$, this can be approximated by:

$$r_{\mathrm{T}}[\mathrm{m}] \approx \frac{p_T[GeV/c]}{0.3 \cdot B[\mathrm{T}]} . \tag{6.1}$$

For the CMS magnetic field strength of $B = 3.8\,\mathrm{T}$, the relationship between the beam incident angle and the transverse momentum of the traversing particle for a radial position R of the module is given by

$$p_T[GeV/c] \approx \frac{0.57 \cdot R[\mathrm{m}]}{\sin(\alpha)} . \tag{6.2}$$

In order to measure the efficiency of the CBC2 correlation logic and the generation of stub triggers in the most unbiased manner possible, no selection requirements were applied to the DUT. The following selection criteria were only applied to the REF:

- exactly one cluster on each of the two sensors (S2 and S3),
- the width of both clusters must be $w \leq 3$ strips,
- cluster positions X must be at least 4 strips away from masked strips,

2018 JINST 13 P03003

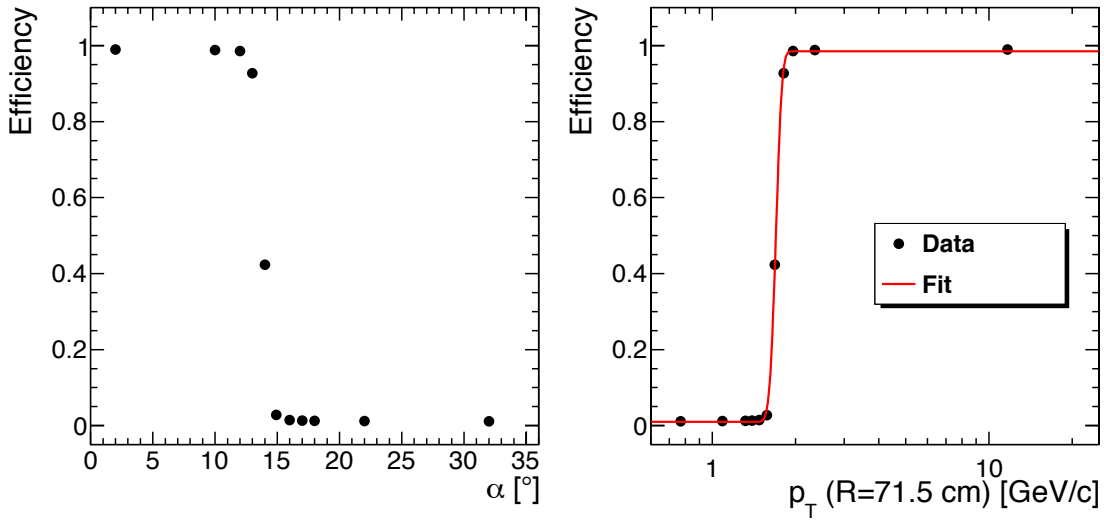

Figure 18. Stub trigger efficiency of the DUT as a function of beam incident angle (left) and as a function of p_T calculated for a radial position of $R = 71.5$ cm in the CMS tracker (right).

- cluster positions X must be at least 30 strips away from the module edges, ensuring the potential track was in the active sensor area even for higher rotation angles,
- the offline stub direction must be $|\Delta X| < 2$ strips.

The purpose of these selection criteria was to reject events where particles were traversing the setup at oblique angles instead of approximately parallel to the beam axis, thereby underestimating the apparent efficiency. In addition, events where an interaction might have occurred just upstream of the DUT, leading to a possible fake correlation, can be rejected with these criteria, providing adequate rejection of background. The efficiency was then defined as the number of stub trigger events from the DUT divided by the total number of selected events.

The beam incident angle is related to the stub direction ΔX, the strip pitch p and the sensor separation d via $\tan(\alpha) = p\Delta X/d$. The CBC2s on the DUT were configured to generate stub triggers using a window size of ±7 strips. According to geometric expectations, for the known pitch of 90 µm and the estimated sensor separation of 2.72 mm, the efficiency should be constant and high for small angles, should start dropping at $\Delta X = 7$, corresponding to $\alpha \approx 13.0°$, and reach values around 0 for $\Delta X = 8$, corresponding to $\alpha \approx 14.8°$. The efficiency as a function of α is shown in figure 18 (left); it is in good agreement with the geometric predictions. The efficiency for $\alpha > 15°$ is close to, but not exactly, zero, and the origin of these stubs is yet to be understood. Interactions in the upstream sensor such as multiple Coulomb scattering or delta rays could partially explain this effect but further measurements in a controlled test beam environment with different particle species are required. More realistic full-sized 2S modules are being evaluated at a CERN beam-line this year which will allow for a more systematic study of this feature. For $\alpha \leq 12°$ the CBC2 stub-finding logic is able to trigger on positrons with about 99% efficiency.

The DUT is a prototype with sensors similar to the recent tracker design, but the sensor spacing of the prototype $d = 2.72$ mm is different from the design sensor spacing of $d_{\text{des}} = 1.8$ mm for the

2018 JINST 13 P03003

outermost barrel layer of the outer tracker. To demonstrate the effective stub trigger efficiency for a module with a design radial position of $R_{\text{des}} = 108\,\text{cm}$, corresponding to the design outermost tracker layer, the effective p_T was calculated from eq. (6.2) for a radius of $R = 71.5\,\text{cm}$, where R was evaluated by scaling the design value with the sensor spacing ratio, $R = R_{\text{des}} \cdot d_{\text{des}}/d$. The effective stub trigger efficiency as a function of p_T is illustrated in figure 18 (right). Due to the beam divergence, the p_T equivalent is slightly smeared out relative to the ideal equations given above, as the tracks are not all perfectly parallel. A similar effect will also appear in the future tracker, as tracks of the same p_T have different incident angles for different positions in the module, which can be partially compensated by the offset correction in the online stub correlation logic, as explained in sections 2.1 and 2.2.

Fitting the efficiency curve allowed extraction of the effective p_T selection threshold and its resolution. The fit function was based on the shifted and scaled error function described by four parameters: the mean value ${p_T}^{\text{trig}}$ corresponding to the effective p_T trigger threshold, the width σ^{trig} corresponding to the resolution of the threshold value, and the asymptotic minimum and maximum efficiencies ϵ_{min} and ϵ_{max}, respectively. The fitted efficiencies yielded $\epsilon_{\text{min}} \approx 1\%$ and $\epsilon_{\text{max}} \approx 99\%$. The module would be able to reject hits from particles below ${p_T}^{\text{trig}} \approx 1.70\,\text{GeV/c}$ with a resolution of $\sigma^{\text{trig}} \approx 0.07\,\text{GeV/c}$. This would allow the CBC2 to suppress the large amount of data from low-p_T tracks present in CMS and only pass hits from high transverse momentum candidates to L1 for further processing.

7 Summary

The future CMS tracker foreseen for the HL-LHC must provide information on tracks of high transverse momentum to the first level trigger, which will be realised by two closely-spaced parallel silicon sensors on each module, using fast correlation logic. Fully functional mini-prototypes of 2S-p_T modules using CBC2s for readout have been analysed for the first time in a test beam. After commissioning, the performance was found to be in agreement with expectations. The cluster width is in good agreement with geometric predictions, and the fraction of very broad clusters is below 1%.

The simultaneous usage of two modules allowed the selection of events where most probably exactly one beam particle traversed all four sensors, and also enabled track predictions that were used for efficiency estimates. The cluster efficiency is almost uniform amongst all tested sensors and chips, and can be kept above 99% without introducing significant noise.

For the first time, the trigger logic of such modules could be tested, by emulating the p_T-dependent track bending in the magnetic field via a rotation of the module. The trigger efficiency shows the desired behaviour. The efficiency to identify high-p_T tracks is around 99%. The separation from low-p_T tracks is excellent; particles with momentum below 1.70 GeV/c could be rejected with a resolution of about 0.07 GeV/c.

Acknowledgments

The measurements leading to these results have been performed at the Test Beam Facility at DESY Hamburg (Germany), a member of the Helmholtz Association (HGF). We acknowledge the support

2018 JINST 13 P03003

from the Belgian Fonds de la Recherche Scientifique. This work is partly supported by the IISN conventions 4.4503.12 and 4.4504.12. The U.K. groups gratefully acknowledge financial support from the Science and Technology Facilities Council. The authors from the Saha Institute of Nuclear Physics acknowledge the Department of Atomic Energy and the Department of Science and Technology for financial support. IPHC authors acknowledge Institut National de Physique Nucléaire et de Physique des Particules (IN2P3) and Centre National de la Recherche Scientifique (CNRS) for financial support.

References

[1] G. Apollinari, I. Béjar Alonso, O. Brüning, M. Lamont and L. Rossi, *High-Luminosity Large Hadron Collider (HL-LHC): Preliminary Design Report*, CERN-2015-005 (2015).

[2] CMS collaboration, *Technical Proposal for the Phase-II Upgrade of the CMS Detector*, CERN-LHCC-2015-010, LHCC-P-008, CMS-TDR-15-02 (2015).

[3] CMS collaboration, *The CMS Experiment at the CERN LHC*, 2008 *JINST* **3** S08004.

[4] Collaboration, *The Phase-2 Upgrade of the CMS Tracker*, CERN-LHCC-2017-009, CMS-TDR-014 (2017).

[5] G. Hall, D. Newbol, M. Pesaresi and A. Rose, *A time-multiplexed track-trigger architecture for CMS*, 2014 *JINST* **9** C10034.

[6] ATLAS collaboration, *The ATLAS Experiment at the CERN Large Hadron Collider*, 2008 *JINST* **3** S08003.

[7] N. Lehmann et al., *Real time tracker based upon local hit correlation circuit for silicon strip sensors*, *Nucl. Instrum. Meth.* **A 806** (2016) 21.

[8] M. Raymond et al., *The CMS binary chip for microstrip tracker readout at the SLHC*, 2012 *JINST* **7** C01033.

[9] W. Ferguson et al., *The CBC microstrip readout chip for CMS at the high luminosity LHC*, 2012 *JINST* **7** C08006.

[10] D. Felici, S. Bertazzoni, S. Bonacini, A. Marchioro, P. Moreira and M. Ottavi, *A 20 mW, 4.8 Gbit/sec, SEU robust serializer in 65nm for read-out of data from LHC experiments*, 2014 *JINST* **9** C01004.

[11] C. Soós et al., *System-level testing of the Versatile Link components*, 2013 *JINST* **8** C12044.

[12] CMS collaboration, *First Implementation of a two-stage DC-DC conversion powering scheme for the CMS Phase-2 outer tracker*, 2017 *JINST* **12** C03090.

[13] D. Braga et al., *CBC2: A microstrip readout ASIC with coincidence logic for trigger primitives at HL-LHC*, 2012 *JINST* **7** C10003.

[14] G. Hall et al., *CBC2: A CMS microstrip readout ASIC with logic for track-trigger modules at HL-LHC*, *Nucl. Instrum. Meth.* **A 765** (2014) 214.

[15] G. Blanchot, D. Braga, A. Honma, M. Kovacs and M. Raymond, *Hybrid circuit prototypes for the CMS Tracker upgrade front-end electronics*, 2013 *JINST* **8** C12033.

[16] T. Behnke et al., *Test Beams at DESY*, EUDET-Memo-2007-11..

[17] D. Cussans, *Description of the JRA1 Trigger Logic Unit (TLU), v0.2c*, EUDET-Memo-2009-4..

2018 JINST 13 P03003

[18] EUDET and AIDA collaborations, I. Rubinskiy, *An EUDET/AIDA Pixel Beam Telescope for Detector Development*, *Phys. Procedia* **37** (2012) 923.

[19] P. Vichoudis et al., *The Gigabit Link Interface Board (GLIB), a flexible system for the evaluation and use of GBT-based optical links*, 2010 *JINST* **5** C11007.

[20] G. Bauer et al., *The CMS data acquisition system software*, *J. Phys. Conf. Ser.* **219** (2010) 022011.

[21] G. Bauer et al., *The run control and monitoring system of the CMS experiment*, *J. Phys. Conf. Ser.* **119** (2008) 022010.

[22] M. Prydderch, CBC2 user manual: CBC2 User Guide v1.1, http://www.hep.ph.ic.ac.uk/~dmray/CBC_documentation/CBC2_User_Guide_v1.1.doc

[23] Particle Data Group collaboration, K.A. Olive et al., *Review of Particle Physics*, *Chin. Phys.* **C 38** (2014) 090001.

2018 JINST 13 P03003

The CMS Tracker collaboration

Institut für Hochenergiephysik, Wien, Austria

W. Adam, T. Bergauer, E. Brondolin, M. Dragicevic, M. Friedl, R. Frühwirth[1], M. Hoch, J. Hrubec, A. König, H. Steininger, W. Treberspurg, W. Waltenberger

Universiteit Antwerpen, Antwerpen, Belgium

S. Alderweireldt, W. Beaumont, X. Janssen, J. Lauwers, P. Van Mechelen, N. Van Remortel, A. Van Spilbeeck

Université Libre de Bruxelles, Bruxelles, Belgium

D. Beghin, H. Brun, B. Clerbaux, G. De Lentdecker, H. Delannoy, G. Fasanella, L. Favart, R. Goldouzian, A. Grebenyuk, G. Karapostoli, T. Lenzi, A. Léonard, J. Luetic, T. Maerschalk, A. Marinov, N. Postiau, A. Randle-Conde, T. Seva, P. Vanlaer, D. Vannerom, R. Yonamine, Q. Wang, Y. Yang, F. Zenoni, F. Zhang

Vrije Universiteit Brussel, Brussel, Belgium

S. Abu Zeid, F. Blekman, I. De Bruyn, J. De Clercq, J. D'Hondt, K. Deroover, S. Lowette, S. Moortgat, L. Moreels, Q. Python, K. Skovpen, P. Van Mulders, I. Van Parijs

Université Catholique de Louvain, Louvain-la-Neuve, Belgium

H. Bakhshiansohi, O. Bondu, S. Brochet, G. Bruno, A. Caudron, C. Delaere, M. Delcourt, S. De Visscher, B. Francois, A. Giammanco, A. Jafari, J. Cabrera Jamoulle, J. De Favereau De Jeneret, M. Komm, G. Krintiras, V. Lemaitre, A. Magitteri, A. Mertens, D. Michotte, M. Musich, K. Piotrzkowski, L. Quertenmont, N. Szilasi, M. Vidal Marono, S. Wertz

Université de Mons, Mons, Belgium

N. Beliy, T. Caebergs, E. Daubie, G.H. Hammad

Helsinki Institute of Physics, Helsinki, Finland

J. Härkönen, T. Lampén, P. Luukka, T. Peltola, E. Tuominen, E. Tuovinen

Department of Physics, University of Helsinki, Helsinki, Finland

P. Eerola

Université de Lyon, Université Claude Bernard Lyon 1, CNRS-IN2P3, Institut de Physique Nucléaire de Lyon, Villeurbanne, France

G. Baulieu, G. Boudoul, L. Caponetto, C. Combaret, D. Contardo, T. Dupasquier, G. Gallbit, N. Lumb, L. Mirabito, S. Perries, M. Vander Donckt, S. Viret

Université de Strasbourg, CNRS, IPHC UMR 7178, Strasbourg, France

J.-L. Agram[2], J. Andrea, D. Bloch, C. Bonnin, J.-M. Brom, E. Chabert, N. Chanon, L. Charles, E. Conte[2], J.-Ch. Fontaine[2], L. Gross, J. Hosselet, M. Jansova, D. Tromson

RWTH Aachen University, I. Physikalisches Institut, Aachen, Germany

C. Autermann, L. Feld, W. Karpinski, K.M. Kiesel, K. Klein, M. Lipinski, A. Ostapchuk, G. Pierschel, M. Preuten, M. Rauch, S. Schael, C. Schomakers, J. Schulz, G. Schwering, M. Wlochal, V. Zhukov

2018 JINST 13 P03003

RWTH Aachen University, III. Physikalisches Institut B, Aachen, Germany
C. Pistone, G. Fluegge, A. Kuensken, O. Pooth, A. Stahl

Deutsches Elektronen-Synchrotron, Hamburg, Germany
M. Aldaya, C. Asawatangtrakuldee, K. Beernaert, D. Bertsche, C. Contreras-Campana, G. Eckerlin, D. Eckstein, T. Eichhorn, E. Gallo, J. Garay Garcia, K. Hansen, M. Haranko, A. Harb, J. Hauk, J. Keaveney, A. Kalogeropoulos, C. Kleinwort, W. Lohmann[3], R. Mankel, H. Maser, G. Mittag, C. Muhl, A. Mussgiller, D. Pitzl, O. Reichelt, M. Savitskyi, P. Schuetze, R. Walsh, A. Zuber

University of Hamburg, Hamburg, Germany
H. Biskop, P. Buhmann, M. Centis-Vignali, E. Garutti, J. Haller, M. Hoffmann, R. Klanner, M. Matysek, A. Perieanu, Ch. Scharf, P. Schleper, A. Schmidt, J. Schwandt, J. Sonneveld, G. Steinbrück, B. Vormwald, J. Wellhausen

Institut für Experimentelle Kernphysik, Karlsruhe, Germany
M. Abbas, C. Amstutz, T. Barvich, Ch. Barth, F. Boegelspacher, W. De Boer, E. Butz, M. Casele, F. Colombo, A. Dierlamm, B. Freund, F. Hartmann, S. Heindl, U. Husemann, A. Kornmeyer, S. Kudella, Th. Muller, M. Printz, H.J. Simonis, P. Steck, M. Weber, Th. Weiler

Institute of Nuclear and Particle Physics (INPP), NCSR Demokritos, Aghia Paraskevi, Greece
G. Anagnostou, P. Asenov, P. Assiouras, G. Daskalakis, A. Kyriakis , D. Loukas, L. Paspalaki

Wigner Research Centre for Physics, Budapest, Hungary
F. Siklér, V. Veszprémi

University of Delhi, Delhi, India
A. Bhardwaj, R. Dalal, G. Jain, K. Ranjan

Saha Institute of Nuclear Physics, HBNI, Kolkata, India
S. Dutta, S. Roy Chowdhury

Institute for Research in Fundamental Sciences (IPM), Tehran, Iran
H. Bakhshiansohl, H. Behnamian, M. Khakzad, M. Naseri

INFN Sezione di Bari,[a] Università di Bari,[b] Politecnico di Bari,[c] Bari, Italy
P. Cariola[a], D. Creanza[a,c], M. De Palma[a,b], G. De Robertis[a], L. Fiore[a], M. Franco[a], F. Loddo[a], G. Sala[a], L. Silvestris[a], G. Maggi[a,c], S. My[a,b], G. Selvaggi[a,b]

INFN Sezione di Catania,[a] Università di Catania,[b] Catania, Italy
S. Albergo[a,b], S. Costa[a,b],A. Di Mattia[a], F. Giordano[a,b],R. Potenza[a,b], M.A. Saizu[a,4], A. Tricomi[a,b],C. Tuve[a,b]

INFN Sezione di Firenze,[a] Università di Firenze,[b] Firenze, Italy
G. Barbagli[a], M. Brianzi[a], R. Ciaranfi[a], V. Ciulli[a,b], C. Civinini[a], R. D'Alessandro[a,b], E. Focardi[a,b], G. Latino[a,b], P. Lenzi[a,b], M. Meschini[a], S. Paoletti[a], L. Russo[a,b], E. Scarlini[a,b], G. Sguazzoni[a], D. Strom[a], L. Viliani[a,b]

INFN Sezione di Genova,[a] Università di Genova,[b] Genova, Italy
F. Ferro[a], M. Lo Vetere[a,b], E. Robutti[a]

2018 JINST 13 P03003

INFN Sezione di Milano-Bicocca,[a] Università di Milano-Bicocca,[b] Milano, Italy

M.E. Dinardo[a,b], S. Fiorendi[a,b], S. Gennai[a], S. Malvezzi[a], R.A. Manzoni[a,b], D. Menasce[a], L. Moroni[a], D. Pedrini[a]

INFN Sezione di Padova,[a] Università di Padova,[b] Padova, Italy

P. Azzi[a], N. Bacchetta[a], D. Bisello[a], M. Dall'Osso[a,b], N. Pozzobon[a,b], M. Tosi[a,b]

INFN Sezione di Pavia,[a] Università di Bergamo,[b] Italy

F. De Canio[a,b], L. Gaioni[a,b], M. Manghisoni[a,b], B. Nodari[a,b], E. Riceputi[a,b], V. Re[a,b], G. Traversi[a,b]

INFN Sezione di Pavia,[a] Università di Pavia,[b] Pavia, Italy

D. Comotti[a,b], L. Ratti[a,b]

INFN Sezione di Perugia,[a] Università di Perugia,[b] Perugia, Italy

L. Alunni Solestizi[a,b], M. Biasini[a,b], G.M. Bilei[a], C. Cecchi[a,b], B. Checcucci[a], D. Ciangottini[a,b], L. Fanò[a,b], C. Gentsos[a], M. Ionica[a], R. Leonardi[a,b], E. Manoni[a,b], G. Mantovani[a,b], S. Marconi[a,b], V. Mariani[a,b], M. Menichelli[a], A. Modak[a,b], A. Morozzi[a,b], F. Moscatelli[a], D. Passeri[a,b], P. Placidi[a,b], V. Postolache[a], A. Rossi[a,b], A. Saha[a], A. Santocchia[a,b] L. Storchi[a], D. Spiga[a]

INFN Sezione di Pisa,[a] Università di Pisa,[b] Scuola Normale Superiore di Pisa,[c] Pisa, Italy

K. Androsov[a], P. Azzurri[a], S. Arezzini[a], G. Bagliesi[a], A. Basti[a], T. Boccali[a], L. Borrello[a], F. Bosi[a], R. Castaldi[a], A. Ciampa[a], M.A. Ciocci[a,b], R. Dell'Orso[a], S. Donato[a,c], G. Fedi[a], A. Giassi[a], M.T. Grippo[a,5], F. Ligabue[a,c], T. Lomtadze[a], G. Magazzu[a], L. Martini[a,b], E. Mazzoni[a], A. Messineo[a,b], A. Moggi[a], F. Morsani[a], F. Palla[a], F. Palmonari[a], F. Raffaelli[a], A. Rizzi[a,b], A. Savoy-Navarro[a,6], P. Spagnolo[a],R. Tenchini[a], G. Tonelli[a,b], A. Venturi[a],P.G. Verdini[a]

INFN Sezione di Torino,[a] Università di Torino,[b] Torino, Italy

R. Bellan[a,b], M. Costa[a,b], R. Covarelli[a,b], M. Da Rocha Rolo[a], N. Demaria[a], A. Rivetti[a], G. Dellacasa[a], G. Mazza[a], E. Migliore[a,b], E. Monteil[a,b], L. Pacher[a], F. Ravera[a,b], A. Solano[a,b]

Instituto de Física de Cantabria (IFCA), CSIC-Universidad de Cantabria, Santander, Spain

M. Fernandez, G. Gomez, R. Jaramillo Echeverria, D. Moya, F.J. Gonzalez Sanchez, I. Vila, A.L. Virto

CERN, European Organization for Nuclear Research, Geneva, Switzerland

D. Abbaneo, I. Ahmed, E. Albert, G. Auzinger, G. Berruti, G. Bianchi, G. Blanchot, J. Bonnaud, A. Caratelli, D. Ceresa, J. Christiansen, K. Cichy, J. Daguin, A. D'Auria, S. Detraz, D. Deyrail, O. Dondelewski, F. Faccio, N. Frank, T. Gadek, K. Gill, A. Honma, G. Hugo, L.M. Jara Casas, J. Kaplon, A. Kornmayer, L. Kottelat, M. Kovacs, M. Krammer[1], P. Lenoir, M. Mannelli, A. Marchioro, S. Marconi, S. Mersi, S. Martina, S. Michelis, M. Moll, A. Onnela, S. Orfanelli, S. Pavis, A. Peisert, J.-F. Pernot, P. Petagna, G. Petrucciani, H. Postema, P. Rose, P. Tropea, J. Troska, A. Tsirou, F. Vasey, P. Vichoudis, B. Verlaat, L. Zwalinski

2018 JINST 13 P03003

Institute for Particle Physics, ETH Zurich, Zurich, Switzerland

F. Bachmair, R. Becker, D. di Calafiori, B. Casal, P. Berger, L. Djambazov, M. Donega, C. Grab, D. Hits, J. Hoss, G. Kasieczka, W. Lustermann, B. Mangano, M. Marionneau, P. Martinez Ruiz del Arbol, M. Masciovecchio, M. Meinhard, L. Perozzi, U. Roeser, A. Starodumov[7], V. Tavolaro, R. Wallny, D. Zhu

Universität Zürich, Zurich, Switzerland

C. Amsler[8], K. Bösiger, L. Caminada, F. Canelli, V. Chiochia, A. de Cosa, C. Galloni, T. Hreus, B. Kilminster, C. Lange, R. Maier, J. Ngadiuba, D. Pinna, P. Robmann, S. Taroni, Y. Yang

Paul Scherrer Institut, Villigen, Switzerland

W. Bertl, K. Deiters, W. Erdmann, R. Horisberger, H.-C. Kaestli, D. Kotlinski, U. Langenegger, B. Meier, T. Rohe, S. Streuli

National Taiwan University (NTU), Taipei, Taiwan

P.-H. Chen, C. Dietz, U. Grundler, W.-S. Hou, R.-S. Lu, M. Moya

University of Bristol, Bristol, United Kingdom

D. Cussans, H. Flacher, J. Goldstein, M. Grimes, J. Jacob, S. Seif El Nasr-Storey

Brunel University, Uxbridge, United Kingdom

J. Cole, C. Hoad, P. Hobson, A. Morton, I.D. Reid

Imperial College, London, United Kingdom

G. Auzinger, R. Bainbridge, P. Dauncey, J. Fulcher[9], G. Hall, T. James, A.-M. Magnan, M. Pesaresi, D.M. Raymond, K. Uchida

Rutherford Appleton Laboratory, Didcot, United Kingdom

D. Braga[10], J.A. Coughlan, K. Harder, L. Jones, J. Ilic, P. Murray, M. Prydderch, I.R. Tomalin

Brown University, Providence, U.S.A.

A. Garabedian, U. Heintz, M. Narain, J. Nelson, S. Sagir, T. Speer, J. Swanson, D. Tersegno, J. Watson-Daniels

University of California, Davis, Davis, U.S.A.

M. Chertok, J. Conway, R. Conway, C. Flores, R. Lander, D. Pellett, F. Ricci-Tam, M. Squires, J. Thomson, R. Yohay

University of California, Riverside, Riverside, U.S.A.

K. Burt, J. Ellison, G. Hanson, M. Olmedo, W. Si, B.R. Yates

University of California, San Diego, La Jolla, U.S.A.

R. Gerosa, V. Sharma, A. Vartak, A. Yagil, G. Zevi Della Porta

University of California, Santa Barbara – Department of Physics, Santa Barbara, U.S.A.

V. Dutta, L. Gouskos, J. Incandela, S. Kyre, S. Mullin, H. Qu, D. White

The Catholic University of America, Washington DC, U.S.A.

A. Dominguez, R. Bartek

2018 JINST 13 P03003

University of Colorado Boulder, Boulder, U.S.A.

J.P. Cumalat, W.T. Ford, F. Jensen, A. Johnson, M. Krohn, S. Leontsinis,T. Mulholland, K. Stenson, S.R. Wagner

Fermi National Accelerator Laboratory, Batavia, U.S.A.

A. Apresyan, G. Bolla[†], K. Burkett, J.N. Butler, H.W.K. Cheung, J. Chramowicz, D. Christian, W.E. Cooper, G. Deptuch, G. Derylo, C. Gingu, S. Grünendahl, S. Hasegawa, J. Hoff, J. Howell, M. Hrycyk, S. Jindariani, M. Johnson, F. Kahlid, C.M. Lei, R. Lipton, R. Lopes De Sá, T. Liu, S. Los, M. Matulik, P. Merkel, S. Nahn, A. Prosser, R. Rivera, B. Schneider, G. Sellberg, A. Shenai, L. Spiegel, N. Tran, L. Uplegger, E. Voirin

University of Illinois at Chicago (UIC), Chicago, U.S.A.

D.R. Berry, X. Chen, L. Ennesser, A. Evdokimov, O. Evdokimov, C.E. Gerber, D.J. Hofman, S. Makauda, C. Mills, I.D. Sandoval Gonzalez

The Ohio State University, Columbus, U.S.A.

J. Alimena, L.J. Antonelli, B. Francis, A. Hart, C.S. Hill

Purdue University Calumet, Hammond, U.S.A.

N. Parashar, J. Stupak

Purdue University, West Lafayette, U.S.A.

D. Bortoletto, M. Bubna, N. Hinton, M. Jones, D.H. Miller, X. Shi

The University of Iowa, Iowa City, U.S.A.

P. Tan

The University of Kansas, Lawrence, U.S.A.

P. Baringer, A. Bean, S. Khalil, A. Kropivnitskaya, D. Majumder, G. Wilson

Kansas State University, Manhattan, U.S.A.

A. Ivanov, R. Mendis, T. Mitchell, N. Skhirtladze, R. Taylor

Johns Hopkins University, Baltimore, U.S.A.

I. Anderson, D. Fehling, A. Gritsan, P. Maksimovic, C. Martin, K. Nash, M. Osherson, M. Swartz, M. Xiao

University of Mississippi, Oxford, U.S.A.

J.G. Acosta, L.M. Cremaldi, S. Oliveros, L. Perera, D. Summers

University of Nebraska-Lincoln, Lincoln, U.S.A.

K. Bloom, D.R. Claes, C. Fangmeier, R. Gonzalez Suarez, J. Monroy, J. Siado

Northwestern University, Evanston, U.S.A.

K. Hahn, S. Sevova, K. Sung, M. Trovato

Rutgers, The State University of New Jersey, Piscataway, U.S.A.

E. Bartz, Y. Gershtein, E. Halkiadakis, S. Kyriacou, A. Lath, K. Nash, M. Osherson, S. Schnetzer, R. Stone, M. Walker

2018 JINST 13 P03003

University of Puerto Rico, Mayaguez, U.S.A.
S. Malik, S. Norberg, J.E. Ramirez Vargas

State University of New York at Buffalo, Buffalo, U.S.A.
M. Alyari, J. Dolen, A. Godshalk, C. Harrington, I. Iashvili, A. Kharchilava, D. Nguyen, A. Parker, S. Rappoccio, B. Roozbahani

Cornell University, Ithaca, U.S.A.
J. Alexander, J. Chaves, J. Chu, S. Dittmer, K. McDermott, N. Mirman, A. Rinkevicius, A. Ryd, E. Salvati, L. Skinnari, L. Soffi, Z. Tao, J. Thom, J. Tucker, M. Zientek

Rice University, Houston, U.S.A.
B. Akgün, K.M. Ecklund, M. Kilpatrick, T. Nussbaum, J. Zabel

University of Rochester, Rochester, U.S.A.
B. Betchart, R. Covarelli, R. Demina, O. Hindrichs, G. Petrillo

Texas A&M University, College Station, U.S.A.
R. Eusebi, R. Patel, A. Perloff, K.A. Ulmer

Vanderbilt University, Nashville, U.S.A.
A.G. Delannoy, P. D'Angelo, W. Johns

†: Deceased
1: Also at Vienna University of Technology, Vienna, Austria
2: Also at Université de Haute-Alsace, Mulhouse, France
3: Also at Brandenburg University of Technology, Cottbus, Germany
4: Also at Horia Hulubei National Institute of Physics and Nuclear Engineering (IFIN-HH), Bucharest, Romania
5: Also at Università degli Studi di Siena, Siena, Italy
6: Also at CNRS-IN2P3, Paris, France
7: Also at Institute for Theoretical and Experimental Physics, Moscow, Russia
8: Also at Albert Einstein Center for Fundamental Physics, Bern, Switzerland
9: Now at CERN, European Organization for Nuclear Research, Geneva, Switzerland
10: Now at Fermi National Accelerator Laboratory, Batavia, U.S.A.

2018 JINST 13 P03003